TECHNISCHE UNIVERSITÄT WIEN

ATOMINSTITUT

DIPLOMARBEIT

Characterization of Silicon Photomultipliers for the PERC Experiment

zur Erlangung des akademischen Grades

Diplom-Ingenieur

im Rahmen des Studiums

066 461 Technische Physik

eingereicht von

Johannes Schilberg, BSc
Matrikelnummer: 01612976

ausgeführt am Atominstitut
der Fakultät für Physik der Technischen Universität Wien

Betreuer: **Univ.Prof. Dr. Hartmut Abele**
Mitwirkung:
Univ.Ass.in Dr.in Irina Pradler

Wien, 06. 06. 2024

Unterschrift Student

Unterschrift Betreuer

Danksagung / Acknowledgements

First I would like to express my deepest gratitude to my advisor Univ. Prof. Dr. Hartmut Abele and my co-supervisor Univ. Ass.in Dr.in Irina Pradler for their commitment and support. Additionally, I would like to extend my sincere thanks to Karina Bernert M.Sc. and Univ. Prof. Dr. Bastian Märkisch from TUM as well as Dr.in Marlene Tüchler and Priv.-Doz. Dr. Johann Zmeskal from SMI for providing hardware and sharing their knowledge.

Furthermore, I want to express my appreciation to Alberto Jose Saavedra Garcia and Sebastian Dorer for countless discussions, and pieces of advice and for creating a welcoming and inspiring atmosphere in the office. Additionally, I would like to thank Dr. Joachim Bosina for sharing his knowledge and constantly reminding me to start writing. I would also like to thank everyone else from the Neutron- and Quantum Physics group, whom I haven't mentioned by name, but who was part of the enriching work environment in which this thesis was written.

Abschließend möchte ich mich bei meiner Familie und meinen Freund:innen bedanken, die mich während meines gesamten Studiums und darüber hinaus stets unterstützt haben und eine unermüdliche Energiereserve für mich waren. Außerdem möchte ich meine tiefe Dankbarkeit gegenüber meiner Freundin Anna ausdrücken, die mich nicht nur während der finalen Phase dieser Arbeit ertragen hat, sondern mich unentwegt emotional und technisch unterstützt hat, bei allen Hindernissen die sich ergeben haben.

Eidesstattliche Erklärung

Ich erkläre Eides statt, dass ich meine Diplomarbeit nach den anerkannten Grundsätzen für wissenschaftliche Abhandlungen selbstständig ausgeführt habe und alle verwendeten Hilfsmittel, insbesondere die zugrunde gelegte Literatur, genannt habe.

Weiters erkläre ich, dass ich dieses Bachelorarbeitsthema bisher weder im In- noch Ausland (einer Beurteilerin/einem Beurteiler zur Begutachtung) in irgendeiner Form als Prüfungsarbeit vorgelegt habe und dass diese Arbeit mit der vom Begutachter beurteilten Arbeit übereinstimmt.

June 6, 2024

Unterschrift Student

Kurzzusammenfassung

Die PERC-Anlage (Proton and Electron Radiation Channel), die sich an der Neutronenquelle FRM II der Technischen Universität München (TUM) befindet, dient als saubere Quelle für Neutronenzerfallsprodukte (Protonen und Elektronen). PERC soll zur Bestimmung des Cabibbo-Kobayashi-Maskawa-Quark-Mischungselements (V_{ud}) beitragen, die Korrelationskoeffizienten des freien Neutronenzerfalls (a, A, b, C) messen und über neue effektive Kopplungen nach neuer Physik im TeV-Bereich suchen. Um die Einschränkungen früherer Messungen des freien Neutronenzerfalls zu überwinden, können systematische Effekte auf 10^{-4}-Ebene kontrolliert werden.

Etwa 2% der durch Neutronenzerfall erzeugten Elektronen werden vom Hauptdetektor des PERC zurückgestreut und geben nicht ihre ganze Energie an den Hauptdetektor ab. Um die gewünschte Genauigkeit zu erreichen, ist es wichtig, diese zurückgestreuten Elektronen nachzuweisen. Das Rückstreudetektorsystem besteht aus 2 Detektoren von denen jeder aus etwa 100 Hamamatu SiPM-Arrays (4×4), die mit einem einzigen Szintillator gekoppelt sind. Dies ergibt eine Gesamtmenge von 3200 SiPMs, die für diesen Detektor verwendet werden. Die Charakterisierung der einzelnen SiPMs ist der Schlüssel zum stabilen Betrieb des Detektors und entscheidend für ein gutes Signal-Rausch-Verhältnis (SNR) der gesammelten Daten.

Die in dieser Arbeit vorgestellten Ergebnisse charakterisieren eines dieser 4×4-Arrays. Das Array bietet auch die Möglichkeit, eine Anzahl von SiPMs gemeinsam auszulesen. Aus diesem Grund wurde das Array als einzelne Kanäle (acht verschiedene Kanäle), in Gruppen von vier Kanälen und mit allen 16 SiPMs gleichzeitig ausgelesen. Durch das gleichzeitige Auslesen von vier SiPMs erhöht sich die Signaldauer um etwa den Faktor zwei und für das gesamte Gerät um einen weiteren Faktor zwei. Andererseits verbessert sich das SNR bei dieser kollektiven Auslesung um den Faktor 1.8. Das Rauschniveau wurde für verschiedene Szintillatoren, zunehmenden Bias-Strom, verschiedene Auslesemethoden (individuelle Auslesung, Gruppen von vier SiPMs gleichzeitig, die gesamte Einheit gleichzeitig) und Kabellängen bis zu 1.9 Metern untersucht. Die Ergebnisse dieser Arbeit können bei der Festlegung der Bedingungen für das Rückstreudetektorsystem von PERC helfen.

Abstract

The PERC (Proton and Electron Radiation Channel) facility, located at the neutron source FRM II of the Technical University of Munich (TUM), serves as a clean source of neutron decay products, namely protons and electrons. PERC aims to contribute to the determination of the Cabibbo-Kobayashi-Maskawa quark-mixing element (V_{ud}), measure the correlation coefficients of free neutron decay (a, A, b, C) and to search for new physics at the TeV scale via new effective couplings. To overcome the limitations of previous measurements on free neutron decay, systematic effects can be controlled on 10^{-4} level.

About 2% of the electrons created by neutron decay get backscattered by the main detector of PERC and do not deposit their whole energy in the main detector. To reach the desired precision, it is important to detect these backscattered electrons. The backscatter detector system consists of two detectors, each of them consisting of approximately 100 Hamamatu SiPM arrays (4×4) coupled to a single scintillator. This gives a total amount of 3200 SiPMs used for this detector system. Characterization of each SiPM is the key to stable detector operation and is crucial for achieving a good Signal-to-Noise Ratio (SNR) of the collected data.

The results presented in this thesis characterize one of these 4×4 arrays. The array also brings the opportunity to read out a number of SiPMs collectively. Because of this, the unit has been read out as individual channels (eight different channels), in groups of four channels, and with all 16 SiPMs simultaneously. Reading out four SiPMs simultaneously increases the signal duration by approximately a factor of two, and for the whole unit, it is increased by another factor of two. On the other hand, the SNR improves with this collective readout by a factor of 1.8. The level of noise has been investigated for different scintillators, increasing bias current, different readout methods (individual readout, groups of four SiPMs simultaneous, the whole unit simultaneous), and cable lengths up to 1.9 m. The results of this work can help with setting up conditions for the backscatter detector system of PERC.

Contents

1. Introduction

The Standard Model (SM) of particle physics describes the known fundamental particles and the forces acting between them. Although the success of the SM is undisputed, it is not a complete description of the universe. While the SM successfully describes the behaviour of known particles and three of the four fundamental forces (electromagnetic, weak, and strong), it fails to explain the gravitational force or the existence of dark matter and dark energy, which are crucial components for understanding the large-scale structure and dynamics of the universe. This incompleteness raises the question towards physics beyond the Standard Model (BSM).

Two approaches have become established for this search for BSM physics: On the one hand, there are high-energy experiments that use the $\mathcal{O}$ (TeV) scale to look for rare decays, new interactions, or new particles. One of the significant contributions of high-energy experiments, notably those at the Large Hadron Collider (LHC), to the SM, was the discovery of the Higgs boson, illuminating the mechanism by which elementary particles acquire mass and validating the theoretical framework of the Higgs field [1, 2]. On the other hand, high-precision experiments at low energies ($\mathcal{O}$(meV)) focus mainly on probing the properties of known particles and interactions. These experiments search for deviations at meV energy scales, which could hint towards BSM physics.

The free neutron decay serves as a powerful probe into the structure of the weak interaction for possible scalar or tensor contributions to the V-A theory of the SM (mediated by vector (V) and axial-vector (A) currents), as described among others by Gorchtein et al. [3]. In addition to that, there is still a discrepancy between the experimentally obtained values for the neutron lifetime τ_n, which depends strongly on the experimental setup used to obtain the lifetime. The two methods to obtain the neutron lifetime are beam measurements with $\tau_n = 888.0 \pm 2.0\,\mathrm{s}$ [4] and magnetic bottle measurements with $\tau_n = 879.4 \pm 0.6\,\mathrm{s}$ [4], which show a discrepancy between these two methods of 8.6 s or 4.1 σ. This discrepancy is visualized in Figure With a high-precision measurement of free neutron decay, this discrepancy can be further investigated, which makes such a measurement even more attractive. With the results from these measurements, information on the Cabibbo–Kobayashi–Maskawa (CKM) quark mixing element V_{ud} [6, 7] and possible scalar and tensor couplings in the weak interaction will be derived [8].

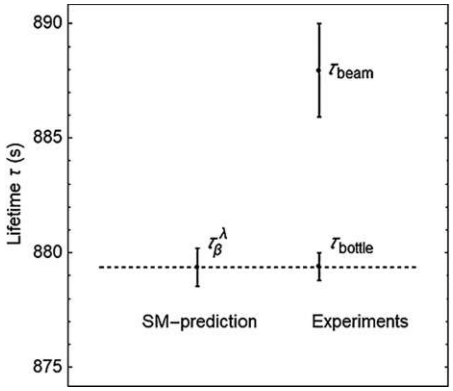

Figure 1.1.: Two different values obtained for the neutron lifetime using different experimental methods. From the beam measurements $\tau_{beam} = 888.0 \pm 2.0\,\mathrm{s}$ is obtained while from the magnetic bottle experiments, one has measured $\tau_{bottle} = 879.4 \pm 0.6\,\mathrm{s}$. Figure taken from [5].

The most precise measurements of the free neutron decay spectrum have been performed with PERKEO III, a large neutron decay spectrometer built by the *Heidelberg Physics Institute*. The main component of PERKEO III is a solenoid coil housing the decay volume, producing a magnetic field of 150 mT, which guides the charged decay products (e^-, p) of thermal neutrons $(\mathcal{O}(25\,\mathrm{meV}))$ to a detector consisting of plastic scintillators and photomultiplier (PMT) [9]. The Flux of decay products at the beam site PF1B of the Institut Laue-Langevin (ILL) was $5 \times 10^4 \mathrm{s}^{-1}$. The spectrum of the electrons coming from neutron decay measured with PERKEO III can be seen in Figure 1.2 PERKEO III also has the most precise measurements of the beta asymmetry parameter $A_0 = -0.11985\,(17)_{stat}\,(12)_{sys.}$ and the nucleon axial coupling $\lambda = -1.27641\,(45)_{stat}\,(33)_{sys.}$ [10, 11]. A comparison of the value for λ obtained by different experiments is given in Figure 1.3.
The precision in measuring free neutron decay has to be increased further to search for new physics at the TeV scale. One upcoming high-precision experiment is PERC (Proton and Electron Radiation Channel) [13, 14], the successor of PERKEO III. PERC is a collaboration of the Universities of Heidelberg and Mainz, the Technical University of Munich, TU Wien and the Institut Laue-Langevin, Grenoble. The PERC facility, located at the neutron source FRM II of the Technical University of Munich (TUM), serves as a clean source of neutron decay products $(10^6 \mathrm{s}^{-1})$ coming from cold neutrons, namely protons and electrons. The decay volume itself is a 8 m long neutron guide surrounded by a solenoid generating a magnetic field of 0.5 - 1.5 T. A schematic of PERC can be seen in Figure 1.4.

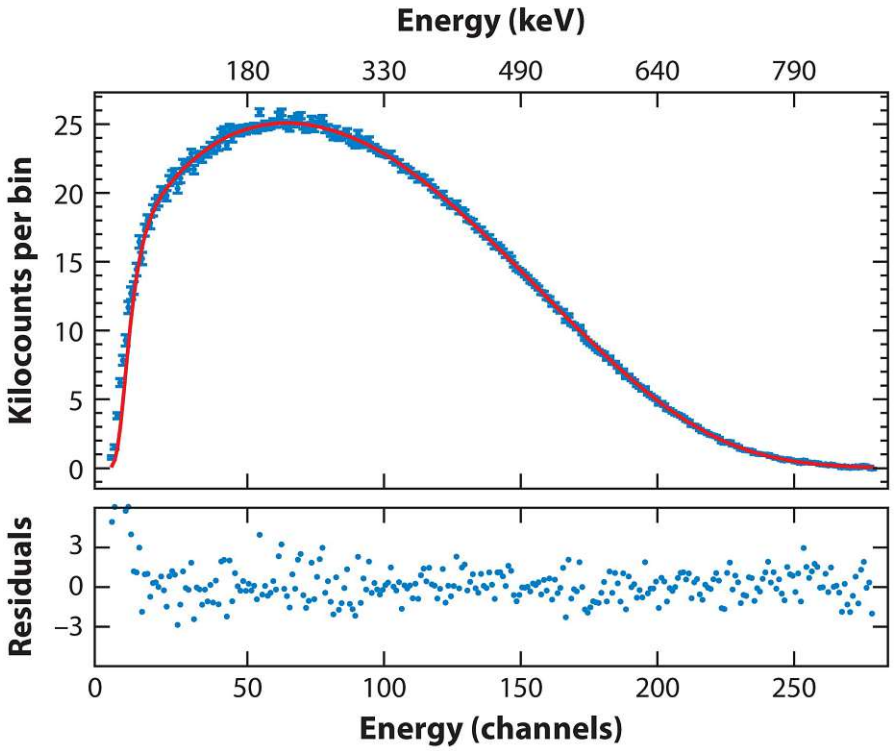

Figure 1.2.: Continuous electron energy spectrum of free neutron decay measured with PERKEO III. The endpoint of the spectrum lies at 782 keV - the maximum energy available for an electron originating in neutron decay. The blue points represent the measured data, and the red line is a fit of the data. Taken from [12].

After the decay volume, the decay products will be separated from the beam by the *e,p selector* - a section designed for this purpose reaching 3.0 - 6.0 T. This field guides the neutron decay products to the downstream detector. As a whole, the main device is a 12 m long superconducting magnet, guiding the neutrons and the neutron decay products to the main detector.
Not all electrons deposit their whole energy in the main detector. Monte Carlo simulations show that about 2% of the electrons do not reenter the main detector after getting reflected back upstream by the main detector [15]. To achieve a precision at which systematic effects can be controlled on 10^{-4} level, the necessity arises to detect these backscattered electrons and prevent them from influencing the measured energy spectrum by being counted as electrons of lower energy. The backscattered electrons get guided back upstream by the magnetic field, where the backscatter detector system will be located. This backscatter detector system is

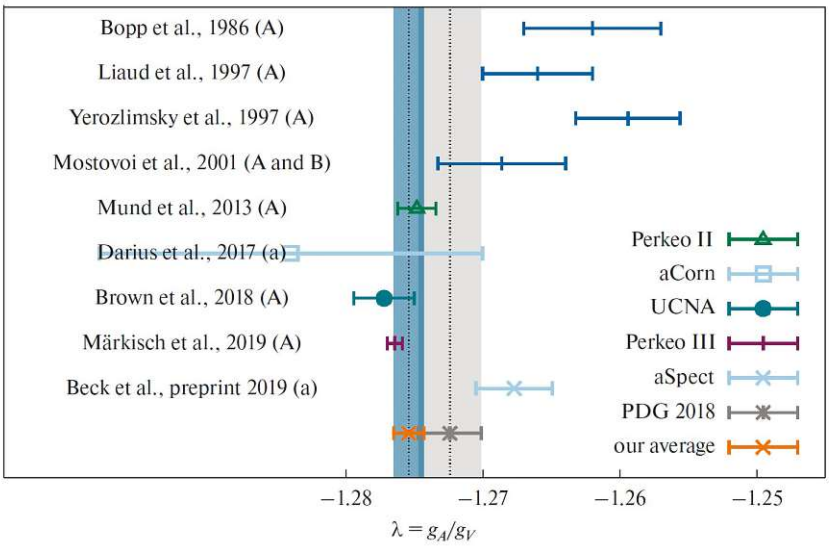

Figure 1.3.: From the data of PERKEO III, a new world average of the ratio of coupling constants $\lambda = \frac{g_V}{g_A} = -1.2754(11)$ has been determined. Figure taken from [11].

currently being developed by a group of TUM [15, 16].
This detector system will consist of two plastic scintillators and an (10×10) array of Hamamatsu *Silicon Photo Multiplier* (SiPM) units on the backside to absorb the scintillation light. Figure 1.5 shows a schematic of the backscattering detector setup. One single unit consists of 4×4 SiPM which means that the backscatter detector system will consist of 3200 individual SiPM.

This thesis aims to characterize one Hamamatsu (4×4) SiPM unit. Since each of the 16 SiPMs of this unit can be biased individually, it is crucial to understand how they differ in their response. One also has the opportunity to read multiple SiPMs out collectively in a group size based on demand. Since the bias voltage also directly influences the pulse shape and, therefore, the spectrum, the response to different overvoltages is characterized as well. Different readout options will be discussed, and their influence on the pulse shape and noise level will be investigated. Other aspects that change the signal-to-noise ratio (SNR) of the SiPM unit are the light output and the scintillation decay times of different scintillators. To investigate this, measurements with different scintillation materials (YSO, BGO, BC-408) have been performed. The SNR depends on the stability of the applied voltage and of the gain. The gain of the system is temperature dependent, therefore, the effect of the temperature response of a SiPM has been investigated with the help of an in-house cooling setup.

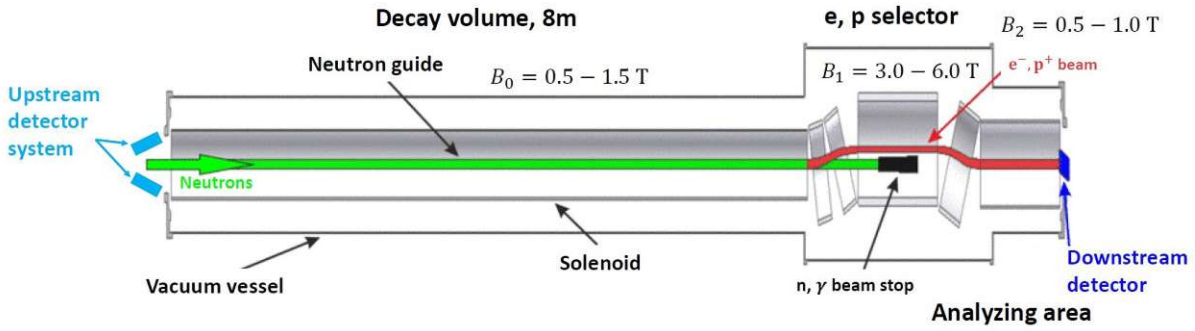

Figure 1.4.: Schematic of the PERC experiment [8]. The green line represents the neutron guide with a beam stop at the end of it. The red section visualizes the path of the charged decay products that will be measured by the backscatter detector (dark blue). The main is located on the other side, marked in light blue.

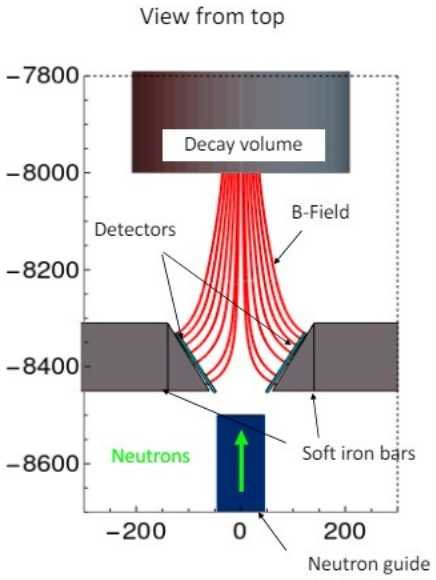

Figure 1.5.: Schematic of the position of the backscattering detector. The detectors will be placed just outside of the decay volume. The two soft iron bars shape the magnetic field to guide the electrons left and right to a detector. Figure is taken from [15]

1.1. Free Neutron Decay

The process known as β-decay is the decay of a nucleon by coupling one of its quarks to a W^+- or a W^--boson, which changes the flavour of the quark during the interaction. This is mediated via the weak interaction of the SM, which allows quarks to change their flavour. Depending on the participating W-boson, one refers to the interaction as β^+- or β^--decay. β^--decay describes the conversion of a neutron into a proton, an electron, and an electron antineutrino:

$$\beta^- \; : \quad n \to p + e^- + \bar{\nu}_{e^-} \tag{1.1}$$

The W^--boson couples to the down-quark (d) of the neutron (udd), therefore changing its flavour to an up-quark (u) by emitting an electron and an electron antineutrino. The remaining quark configuration (uud) is the emitted proton. Fermi first described the underlying concept in 1933 [17]. The corresponding Feynman diagram of the β^--decay can be seen in Figure 1.6.

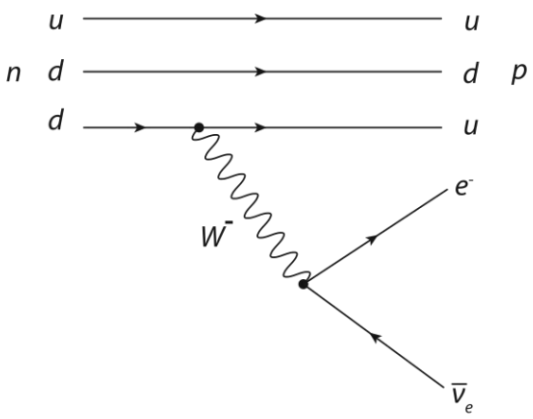

Figure 1.6.: Feynman diagram of the β^--decay of a free neutron. The W^--boson couples to the down-quark (d) of the neutron (udd), therefore changing its flavour to an up-quark (u) by emitting an electron and an electron antineutrino. The remaining quark configuration (uud) is the emitted proton.

The available energy for the decay of the free neutron is given by the mass difference [18] between the interacting particles:

$$E_{\beta^-} = m_n - m_p - m_e = 782.333\,41(46)\,\text{keV} \tag{1.2}$$

At this energy scale, it is possible to describe the interaction as a four-fermion interaction [19]. Using the Fermi theory one can derive a differential decay rate

for the neutron decay [20], neglecting electromagnetic interaction and integrating over angular dependencies:

$$\mathrm{d}\Gamma = \frac{G_F^2 |V_{ud}|^2}{32\pi^5} \left(1 + 3\lambda^2\right) p_e E_e (E_{\beta^-} - E_e)^2 \mathrm{d}E_e \tag{1.3}$$

with Fermi constant G_F, the momentum p_e and the energy of the electron E_e, the CKM quark mixing element V_{ud} and λ, the ratio of axial vector coupling g_A and the vector coupling g_V of weak interaction. Following the field theory approach, one can formulate a Lagrangian for nuclear beta decay transitions and use Fermi's golden rule to reformulate the decay rate in a way that is better suited for experimental neutron physics.

As shown in the paper of J. D. Jackson et al. [21], the decay rate of a free neutron is given by:

$$\begin{aligned} \mathrm{d}^3\Gamma = \frac{1}{2\pi} \frac{G_F^2 {V_{ud}}^2}{2} p_e E_e (E_0 - E_e)^2 \mathrm{d}E_e \mathrm{d}\Omega_e \mathrm{d}\Omega_\nu \\ \xi \left[1 + a \frac{\vec{p}_e \vec{p}_\nu}{E_e E_\nu} + b \frac{m_e}{E_e} + \frac{\vec{s}_n}{s_n} \left(A \frac{\vec{p}_e}{E_e} + B \frac{\vec{p}_\nu}{E_\nu} + D \frac{\vec{p}_e \times \vec{p}_\nu}{E_e E_\nu} \right) \right] \end{aligned} \tag{1.4}$$

with the momenta of the electron p_e and the neutrino p_ν, their energies E_e and E_ν, the mass of the electron m_e, the spin of the neutron s_n, the CKM matrix element V_{ud} and the maximum kinetic energy of the electron E_0. The parameters ξ, a, b, A, B, D are the so-called correlation coefficients of free neutron decay and depend on the complex coupling coefficients. They have been given different names based on their physical interpretation: a is the electron-neutrino correlation coefficient, b the Fierz-Term, A the β-asymmetry coefficient, B the neutrino asymmetry coefficient and D the triple correlation coefficient. In the SM, the Fierz term is zero. Table 1.1 gives an overview of these coefficients. As shown in the paper of Saul et al. [22] the Fierz-Term b, under consideration of possible scalar (g_s) or tensor coupling (g_T) in addition to the V-A theory of the SM, can be written as a function of the coupling constants:

$$b \approx 2 \, \frac{g_s + 3\lambda g_T}{1 + 3\lambda^2} \tag{1.5}$$

With $\lambda = \frac{g_A}{g_V}$. The other parameters can be expressed as functions of λ as well.

With PERC, parameters a, b, A, C can be directly obtained from single particle spectra [23]. As recently suggested in the paper from Seng [24], one can extend the correlation coefficients of the free neutron decay. By allowing proton polarization, 33 new coefficients can be introduced in addition to the 18 existing ones.

Coefficient	Name
a	Electron-Neutrino Correlation
b	Fierz-Term
A	β-Asymmetry
B	Neutrino Asymmetry
C	Proton Asymmetry
D	Triple Correlation Coefficient

Table 1.1.: Overview of important correlation coefficients and their names.

1.2. Interaction of Radiation with Matter

Radiation interacts with matter by causing excitations and ionizations. Excitation raises an electron of the atom to a higher energy state, while ionization removes electrons, resulting in the formation of ion pairs (a positive and a negative ion) [25]. These interactions transfer energy from the radiation to the matter. The total stopping power describes the loss of kinetic energy that a charged particle experiences due to the interaction with matter [26]. It is defined as follows:

$$S(E) = -\frac{\mathrm{d}E}{\mathrm{d}x} \,, \tag{1.6}$$

with the minus sign for positive values of S. For choosing the right dimensions of a scintillator, it is important to estimate how far an electron needs to travel in the scintillation material to deposit the energy with which it has been emitted. This distance is called the *range*. To calculate the range, one has to multiply the total stopping power $S(E)$ with the density ρ of the scintillation material. Afterwards, one integrates the inverse total stopping power from 0 to the original energy of the particle. Following these steps, one gets the following formula for the range of a particle in a material of density ρ:

$$\Delta x = \rho \cdot \int_0^{E_0} \frac{1}{S(E)} \,\mathrm{d}E \tag{1.7}$$

With the data taken from the *ESTAR* database [27], the stopping power has been plotted for BC-408, YSO, and BGO (see Figures 1.7 - 1.9) to investigate

the behaviour of electrons in the scintillator materials. Additionally, the range of electrons in all these materials has been calculated to see how thick a layer of the material would need to be to stop electrons at a certain energy fully.

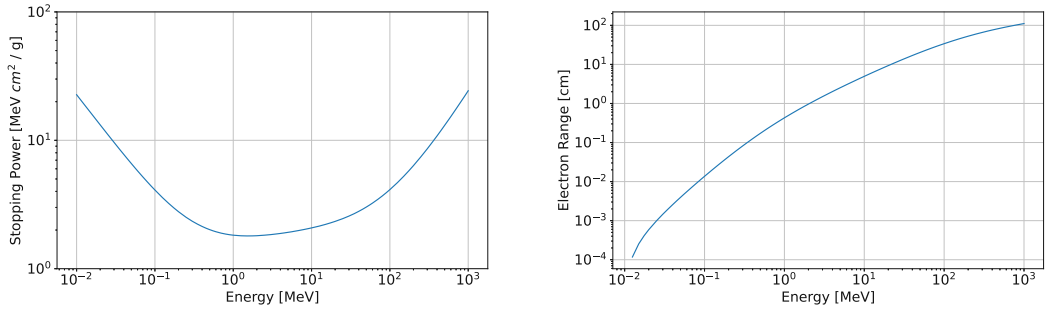

Figure 1.7.: Left: Total stopping power for electrons in BC-408. Right: Range of electrons in BC-408 ($\rho = 1.032\,\mathrm{g\,cm^{-3}}$). Data taken from [28].

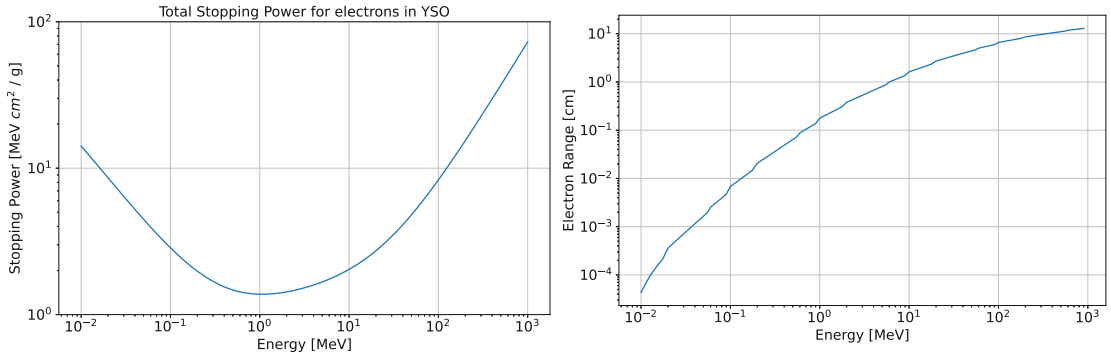

Figure 1.8.: Left: Total stopping power for electrons in YSO. Right: Range of electrons in YSO ($\rho = 4.5\,\mathrm{g\,cm^{-3}}$). Data taken from [28].

To stop electrons with an energy of 1 MeV, a BC-408 plastic scintillator would need a thickness of approximately 5 mm, as one can see in Figure 1.9. To fully absorb electrons of the same energy, a YSO scintillator would need to be at least 2 mm thick and for BGO already 1 mm is sufficient to stop 1 MeV electrons. The energy assumed for these values (1 MeV) is higher than the highest possible energy of an electron coming from neutron decay (782 keV), therefore the calculated thicknesses are sufficient to stop electrons produced by the decay of a free neutron.

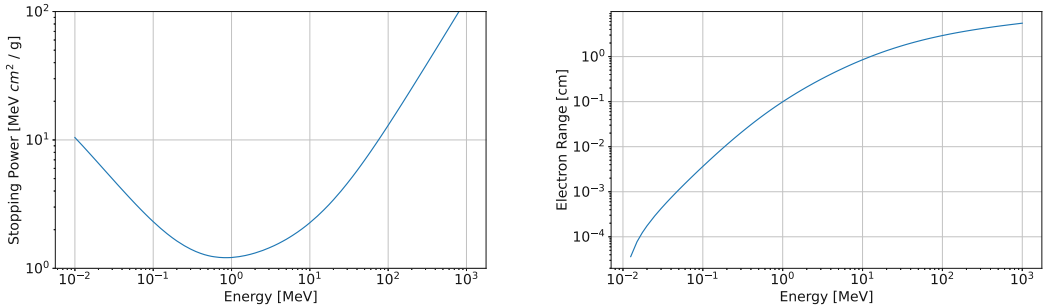

Figure 1.9.: Left: Total stopping power for electrons in BGO. Right: Range of electrons in BGO ($\rho = 7.3\,\mathrm{g\,cm^{-3}}$). Data taken from [28].

For photons at energies below 1 MeV the relevant interactions with matter are the photoelectric effect and Compton scattering. The photoelectric effect typically occurs for photons with energy <0.1 MeV. When a photon with sufficient energy interacts with an electron in an atom, it can transfer enough energy to the electron to overcome the work function of the material and eject the electron from the atom [29]. Subsequently, an electron from a higher energy level can fall into the lower energy level left by the ejected electron, emitting a photon corresponding to the energy difference between these levels. Above 0.1 MeV the dominant interaction of photons with matter is Compton scattering. Compton scattering describes the inelastic scattering of a high-energy photon (γ) by a free or weakly bound electron, resulting in a transfer of energy from the photon to the electron. This interaction causes the electron, known as a Compton electron, to be ejected, while the photon loses energy. The ejected electron travels through the surrounding medium, creating ion pairs similar to a beta particle of equivalent energy. Pair production is not relevant for gammas below 1 MeV.

2. Experimental Setup

The goal of this work was to characterize the stability of SiPM detectors and the effect of different operation conditions on the SNR. In this chapter, all equipment of the experimental setup used in the measurements will be presented. Figure 2.1 shows a schematic of this setup:

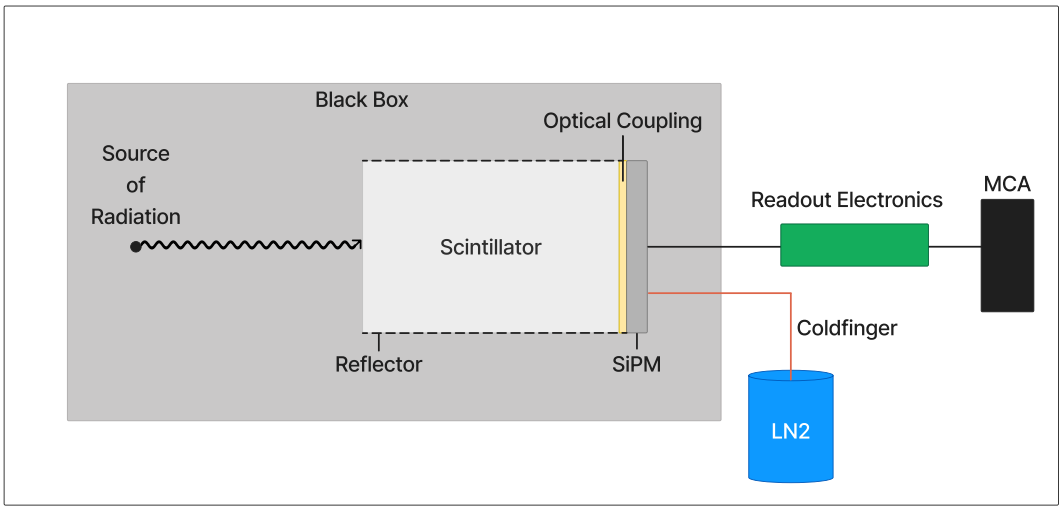

Figure 2.1.: Schematic of the setup used for the characterization of the SiPMs. A radioactive source is placed inside of a black box. The emitted radiation gets absorbed by a scintillator, which converts the absorbed energy into light. This light is guided via an optical coupler toward the SiPM. In the SiPM, the light triggers an avalanche of photoelectrons, which results in a current pulse. This voltage pulse is then shaped and amplified by the readout electronics and either the pulse itself is recorded via an oscilloscope, or the pulses of different sizes are counted by an MCA, resulting in a spectrum. A coldfinger can be connected to the system to control the temperature of the detection system.

A radioactive source is placed in front of a scintillator wrapped in a reflective layer. The scintillation light caused by the particles, emitted from the source and absorbed by the scintillator, is guided via an optical coupler towards a SiPM,

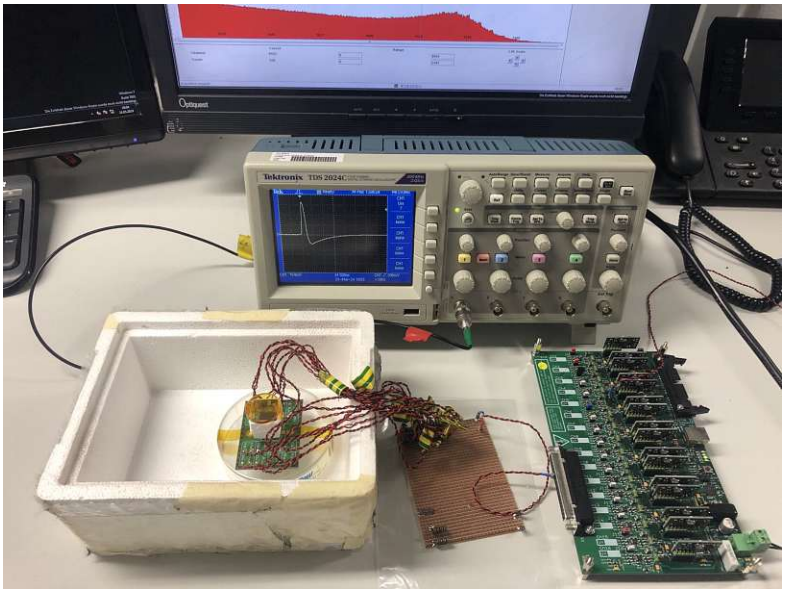

Figure 2.2.: Part of the setup used for the Measurements. The styrofoam box is the lower part of the black box, with the source, scintillator and SiPM inside of it. The readout electronics stand on the right side of the box with an oscilloscope showing a recorded pulse in the background.

where the light gets converted into a current pulse. To prevent external light from disturbing the measurements, this entire part of the setup has been placed inside a black box. A twisted pair of cables forwards the pulse to the readout electronics outside the black box, where the pulse is shaped and amplified. An ADC then converts the analog signal from the readout electronics into a digital signal that can be processed by a Multi-Channel Analyzer (MCA). These amplified pulses can then be directly recorded with an oscilloscope or sorted by their pulse height with an MCA to obtain a spectrum. Figure 2.2 shows parts of the setup in use.

2.1. SiPMs

A Silicon Photomultiplier (SiPM), also referred to as multi-pixel photon counter - MPPC, or Geiger-mode avalanche photodiodes - G-APDs, is a solid state photomultiplier with a multi-pixel structure [30–32]. SiPMs are based on the SPAD technology (Single-Photon Avalanche Diodes), meaning they consist of an array with a high number of single SPADs. A SPAD uses the principle behind a regular photodiode, which is to use a p-n junction to create electron-hole pairs out of an entering electron. The electrons and holes are then accelerated in different directions, which results in a current and the growth of a depletion zone [33,

34]. A SPAD accelerates the electrons and holes with high electric fields, which causes impact ionisations and, therefore, secondary charge carriers [35]. The voltage at which the behaviour changes from a linear multiplication to an exponential avalanche is called breakdown voltage (V_{bd}) [30]. If the bias voltage is higher than the breakdown voltage, the SPAD works in Geiger mode. The secondary carriers can then again ionize particles and so on. This results in the creation of an exponential avalanche and, therefore, a strong electric signal caused by a single photon. The principle of such a SPAD is displayed in Figure 2.3:

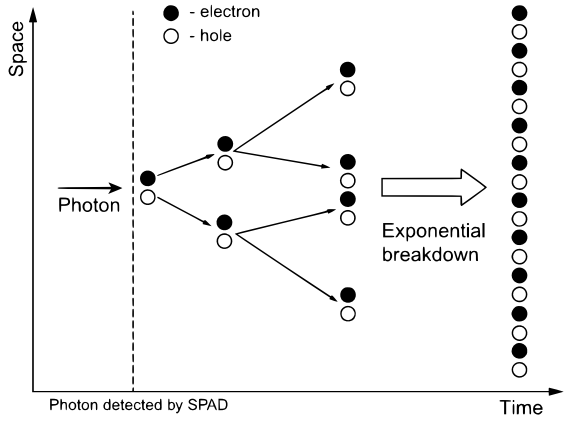

Figure 2.3.: Illustration of a single Photon causing an avalanche in a single-photon avalanche diode (**SPAD**). Figure taken from [35].

Since a SPAD is sensitive to single photons for wavelengths of 450-1000 nm and a SiPM is an array of SPADs, this leads to a very high photodetection efficiency ($\mathcal{O}(40\ \%)$) [36, 37]. Additionally, SiPMs also come with a gain comparable to a PMT (photomultiplier tube) and very good timing properties in the order of 10 ps [38]. The gain of a SiPM can reach from 10^5 up to 10^7 [39]. Therefore, and since SiPMs are not sensitive to magnetic fields, they became a primary choice for man and backscattering detectors instead of the formerly used PMTs. In this work, SiPMs from two different producers and of different dimensions were characterized, namely the AdvanSiD SiPM (NUV) and the Hamamatsu MPPC array (SiPM).

2.1.1. AdvanSiD SiPM (NUV)

One of the scintillation detectors used in the experimental setup is a solid-state Silicon Photo Multiplier (NUV SiPM) with single photon sensitivity from the company AdvanSiD [40]. This SiPM has a very high gain of 3.6×10^6, good timing performance (recharge time constant $\tau_{RC} = 70$ ns), and a low operating voltage V_{op} of the order of $\mathcal{O}(30\,\mathrm{V})$ [41]. Their maximum overvoltage working range,

within which they operate efficiently, lies at 6 V). The photodetection efficiency (PDE) peaks around 420 nm and the operating temperature lies between −25 °C and 40 °C. The exact PDE function is displayed in Figure 2.4.

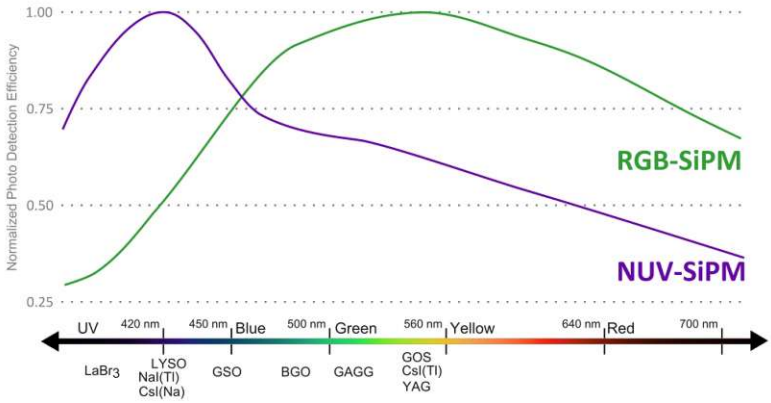

Figure 2.4.: Photo detection efficiency of the AdvanSiD SiPM (NUV). The violet function is the PDE of the SiPM used for the measurements, the green line is for a different product. Figure taken from [41].

To obtain optimal results, it is crucial to maintain a stable temperature since the breakdown voltage changes by 26 mV °C^{-1}. The dimensions of the AdvanSiD SiPM are 4 mm × 4 mm × 1.25 mm, which can be seen in Figure **??**. An overview of the most important parameters of the AdvanSiD SiPM is given in Table 2.1.

Parameter	Symbol	Value	Unit
Breakdown Voltage	V_{Br}	26±2	V
Operating Voltage	V_{Op}	V_{Br}+4	V
Gain	M	3.6×10^6	-
Spectral response range	λ	350-900	nm
Temperature coefficient of recommended operating voltage	$\Delta T\ V_{Op}$	26	mV/°C
PDE at peak	-	43	%

Table 2.1.: Properties of the AdvanSiD SiPM (NUV), taken from the datasheet [41].

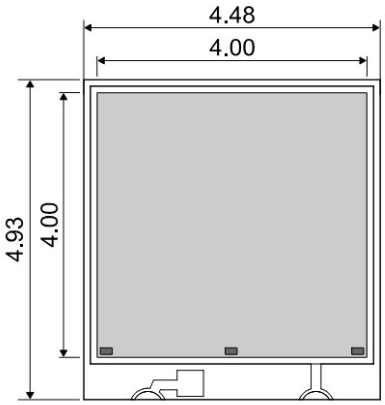

Figure 2.5.: Dimensions of the AdvanSiD SiPM (NUV). Figure taken from [41].

2.1.2. Hamamatsu MPPC Array (SiPM)

One Hamamatsu SiPM array (S13361-3050AE-04) consists of 4×4 SiPMs. The photodetection efficiency (PDE) of the array peaks around 450 nm [41, 42]. The exact PDE is displayed in Figure 2.6. The dimensions of the array are 13 mm × 13 mm × 1.35 mm and the dimensions of an individual SiPM of the array are 3 mm × 3 mm × 1.35 mm. Other important properties can be seen in Table 2.2.

Parameter	Symbol	Value	Unit
Breakdown Voltage	V_{Br}	53±5	V
Operating Voltage	V_{Op}	V_{Br}+3	V
Gain	M	1.7×10^6	-
Spectral response range	λ	320-900	nm
Temperature coefficient of recommended operating voltage	$\Delta T\ V_{Op}$	54	mV/°C
PDE at peak	-	40	%

Table 2.2.: Properties of the Hamamatsu MPPC array (S13361-3050AE-04), taken from the datasheet [43]

The positions of the individual SiPMs are marked with names A1 - D4 in the right picture of Figure 2.6. These abreviations will be used to refer to the position of the individual SiPMs. Figure 2.7 shows the frontside of the array and backside the connector.

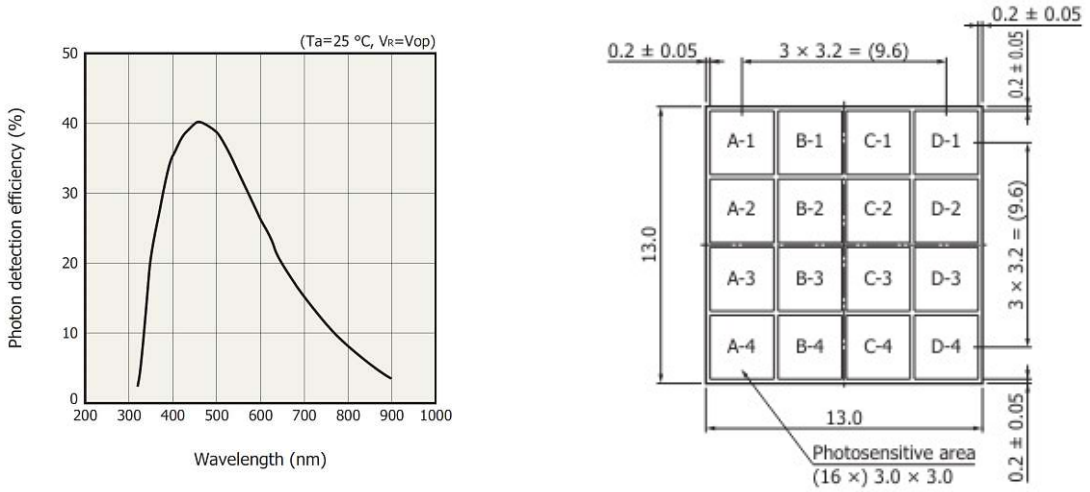

Figure 2.6.: Left: Photodetection efficiency of a Hamamatsu MPPC array. Right: Schematic of the array and the 16 individual SiPMs (A1 - D4). Both pictures are taken from the official data sheet provided by Hamamatsu [43].

Figure 2.7.: Left: Frontside of the array with a 10-cent coin next to it for scale comparison. (SiPM: 13 mm × 13 mm, Coin: $\varnothing = 19.75$ mm)
Right: Backside of the unit showing the connector and the anodes and cathodes of the individual SiPMs.

2.2. Scintillators

A scintillator is a material that emits a flash of light when being hit by a traversing particle or radiation. Scintillation light is emitted after the energy of such a particle is transferred to the scintillator material, causing electronic excitations where electrons are elevated to higher energy states or conduction bands; the subsequent de-excitation process involves the recombination of electron-hole pairs, resulting in the emission of scintillation photons. The amount of scintillation light is proportional to the absorbed energy energy and depends on the particle type. This is described by the ionization density, which is a measure of the number of ionization events per unit length along the path of a particle.

Inorganic and Plastic Scintillators

The scintillators used in this work are inorganic scintillators and a the plastic scintillator. The scintillation mechanism of an inorganic crystal lies in its electronic band structure. There are two ways in which a particle can interact with the inorganic scintillator: it can ionize the crystal by exciting an electron of the valence band or it can create an excitation by exciting an electron to a higher energy band. The ionisation produces a free electron and a free hole; the excitation is a coupled electron-hole pair. The free holes or the hole of an electron-hole pair can now hit impurities and thus ionize these impurities. This leaves an opening a free electron can use to de-excite back into the ground state by emitting a photon.
In a plastic scintillator, particle interactions primarily excite the molecular structure of an aromatic matrix composed of hydrocarbons with conjugated π-electron systems. The energy deposited by the particle raises the π-electrons of the aromatic molecules to higher electronic states. These excited states then transfer energy to fluorescent dopants through non-radiative processes. The dopants, chosen for efficient light emission, de-excite by emitting visible photons. This rapid emission, typically within nanoseconds, makes plastic scintillators suitable for fast-timing applications. Another advantage of plastic scintillators is that they can be produced in larger sizes for a lower price compared to crystal scintillators and are relatively robust. In PERC BC-404 will be used and can be easily produced in large sizes for a moderate price.

Linearity and Temperature Dependency of scintillation output

One can assume that the response of a scintillation crystal to the exciting energy is linear. The light yield of a scintillator per path length is a function of the energy loss per path length of the particle moving through the scintillator. This

relationship is described by the empirical formula called Birks' Law [44, 45]:

$$\frac{\mathrm{d}L}{\mathrm{d}x} = S\frac{\frac{\mathrm{d}E}{\mathrm{d}x}}{1 + kB\frac{\mathrm{d}E}{\mathrm{d}x}} \tag{2.1}$$

$\frac{\mathrm{d}L}{\mathrm{d}x}$ is the light yield per path length, $\frac{\mathrm{d}E}{\mathrm{d}x}$ the energy loss per path length, S the scintillation efficiency, k the quenching probability and B a measure for energy loss due to the density of ionized molecules [45]. The factor kB is also often referred to as *Birks' coefficient*.
Three scintillators have been used in this work:

- YSO crystal scintillator
- BGO crystal scintillator
- BC-408 plastic scintillator

Some important properties of the scintillators are listed in Table 2.3:

	Light Yield [Photons/MeV]	Decay Time [ns]	Density [g/cm^3]	Dimensions [mm]
YSO	10 000-12 000	50-70	4.5	$\varnothing = 5$, Height $= 20$
BGO	8000-10 000	300	7.3	$30 \times 8 \times 4$
BC-408	10 000	2.4	1.05	$18 \times 18 \times 18$

Table 2.3.: Dimensions and properties of the scintillators used for the measurements. Data taken from [46–49].

YSO(Ce) Crystal

YSO(Ce) stands for *Yttrium Orthosilicate:Cerium* (Y_2SiO_5:Ce), and thus, it is a cerium-doped yttrium silicate. The company *Epic-Crystal* [46] produced the crystal used in this work. The cylindric crystal has a diameter of 5 mm and a height of 20 mm and it has the maximum of the emission peak at 420 nm. The light output of the crystal is about 12 000 photons per MeV and the decay time - The duration within which the emitted scintillation light diminishes to a level equivalent to $\frac{1}{\mathrm{e}}$ of its initial maximum - lies between 50 and 70 ns [46, 47].

BGO Crystal

Bismuth Germanate - BGO - is one of the most known heavy scintillators. The high atomic number of Bi and the high density of BGO (7.3 g cm^{-3}) cause the

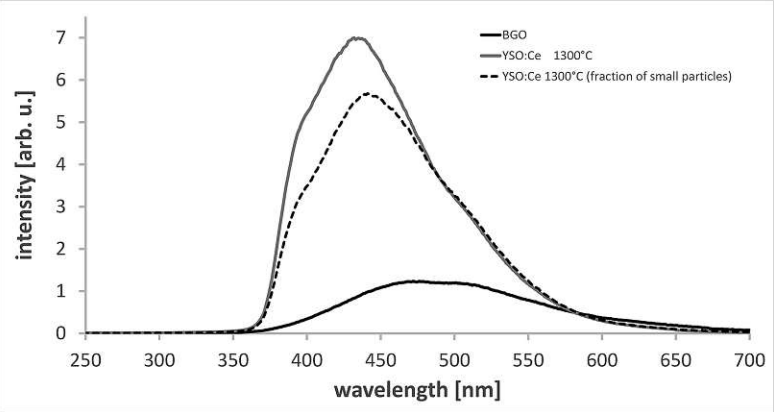

Figure 2.8.: The emission spectra of BGO and YSO. The black line shows the emission spectrum of BGO with an emission peak at around 480 nm. The grey line shows the emission spectrum of YSO with the emission peak at approximately 430 nm. This differs from the value of 420 nm given by the producer of the crystal used in this work, but this is acceptable since the exact peak position is specific for the degree of the Ce doping. Figure taken from [50]

large γ-absorption cross-section [47]. The light yield lies around 8000 photons per MeV [48] and it has a decay time of 300 ns. The Dimensions of the crystal used in this work are: 30 mm × 8 mm × 4 mm. The emission peak of BGO lies at around 480 nm. The emission spectrum is shown in Figure 2.8:

BC-408 Plastic Scintillator

Two main advantages of the BC-408 plastic scintillator are the fast response time in the order on ns and that it can be produced for a reasonable price even in larger dimensions. The decay time given by the producer lies around 2.4 ns [46]. This fast response of the scintillator is of importance for PERC since the reaction time of the backscattering detector is aimed to be in the order of 1 ps. The scintillator has an emission peak around 430 nm which lies again in the middle of the response range of the SiPMs. The dimensions of the plastic scintillator are: 18 mm × 18 mm × 18 mm

Reflector and Optical Coupling

To improve the collection of the emitted scintillation light, all crystals and BC-408 were wrapped in Teflon tape (PTFE). It has a thickness of 0.2 mm [51] and reflects 95% of the reflected light [15]. To optically couple the scintillation light to the SiPM, a silicone waver has been placed between the scintillator and the SiPM.

2.3. Readout Electronics

The simplified process of the signal processing can be seen in Figure 2.9. One

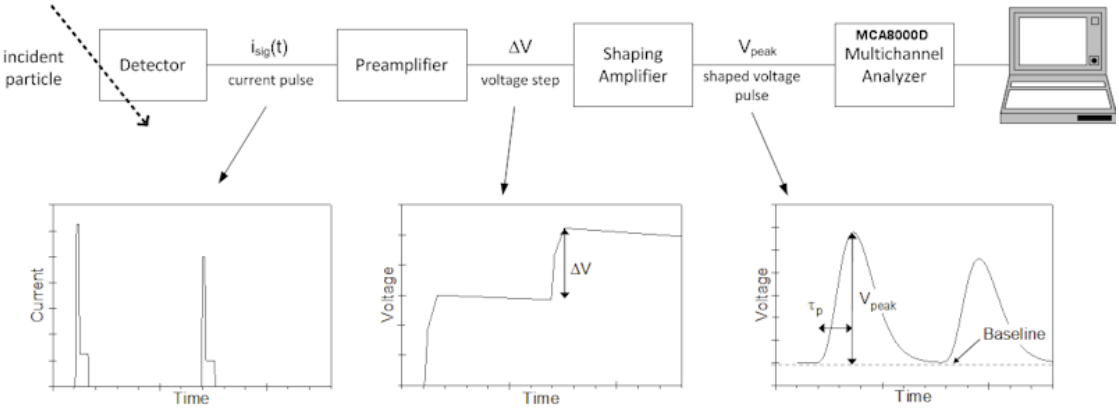

Figure 2.9.: Basic principle behind the signal processing of a SiPM signal. Figure taken from [52].

usually uses a preamplifier to create a voltage step out of the current pulse originating from the incident particle. This voltage step then has to be transformed to a so-called *shaped voltage pulse*, which means that the information about the time in which the original current pulse occurred is now included in the width of the peak. The information about the height and width of the voltage peak is then used by the MCA (*Multichannel Analyzer*) to sort the peaks by voltage and, therefore, by the energy of the incident particle. In the experimental setup used for this work, an amplifying board produced by the Stefan Meyer Institute (SMI) for Subatomic Physics [53] (shown in Figure 2.10) combines the preamplifier and the *shaping amplifier* in one single device. The board also acts as the power supply of the NUV SiPM. It has four different channels, three of them with 70 V bias voltage and one with 30 V. The exact bias voltage/current can be adapted with a potentiometer on each channel. The board has an analogue and a digital (TTL) output. The MCAs used in the measurements are a digital Pocket MCA (MCA8000D) from company Amptek [52] and a MCA-527 from the company GBS Elektronik [54].
For the Hamamatsu array, one needs a different power supply since it is desirable to power and read out all 16 SiPMs at the same time or individually. This power supply was again provided to us by the SMI [53] and can be seen in Figure 2.11. It comes with the important option to power all 16 channels individually, which allows to set bias for all SiPMs differently. The 16 channels all have a potentiometer that allows changing the bias current for each channel depending on requirements. This can be used to compensate for differences in gain or to test the SiPMs under

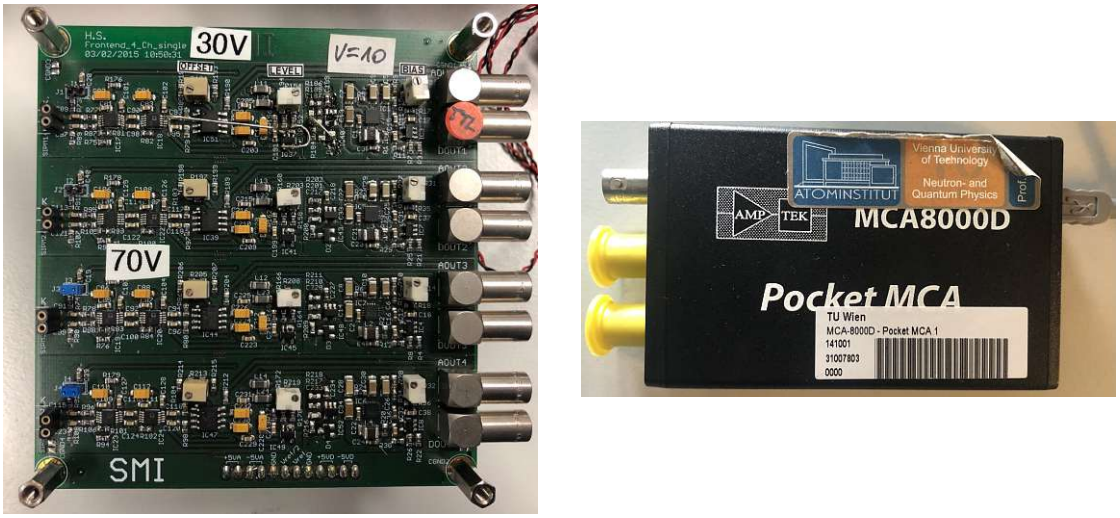

Figure 2.10.: Left: Amplifying board produced by SMI [53]. It consists of four input channels, three of them with 70 V bias voltage and one on them with 30 V. The board has an analogue and a TTL output. Right: MCA (right) used for the measurements of the β- and γ-spectra.

different conditions. The SiPMs are connected via a D-sub connector and biased via the input channels by so-called High-Voltage (HV) modules supplying a voltage of up to 70 V. The gain for the analogue pulse and the voltage threshold for the ToT signal are both adjustable remotely over Universal Serial Bus (USB) [55]. It can be grounded and has analogue and digital (TTL) output. More information on both amplifying boards can be found in [55, 56].

2.3.1. Oscilloscope

The oscilloscope used to record the pulses shown in section 3.2 is a *Digital Storage Oscilloscope TDS2024c* from the company *Tektronix*. More information on this device can be found in the datasheet provided by the company [57].

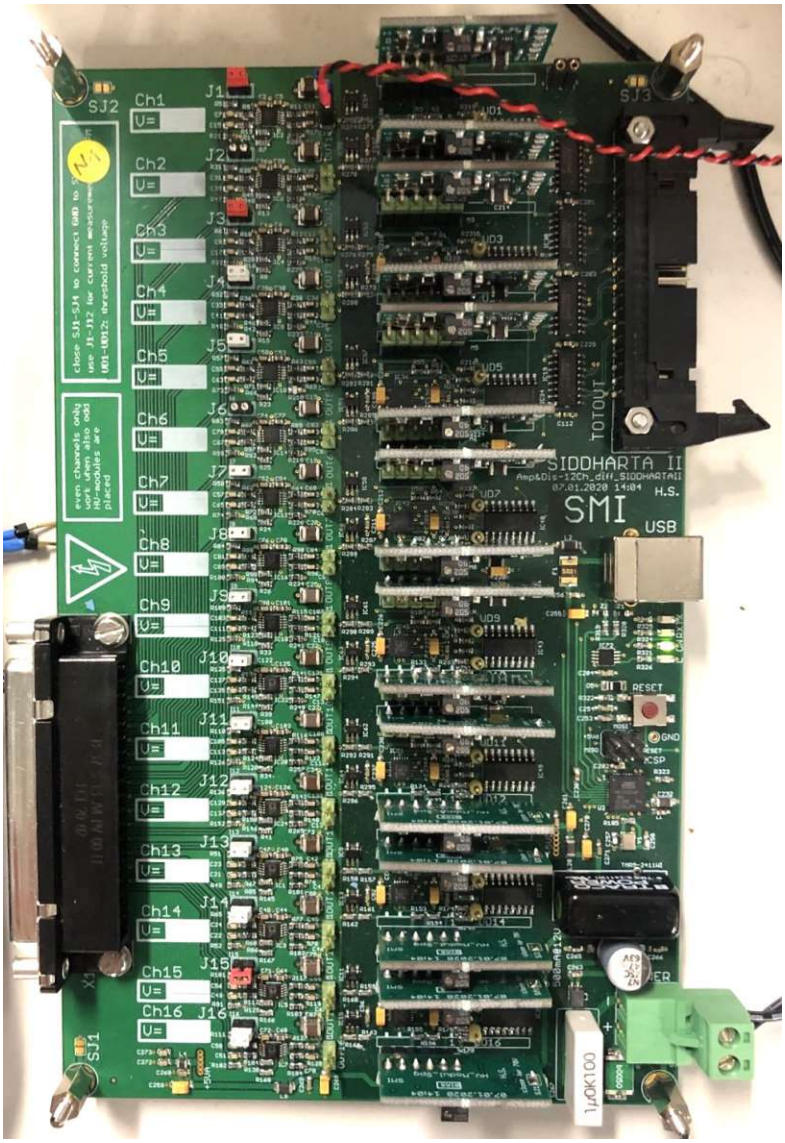

Figure 2.11.: 16 channel amplifying board produced by SMI [53]. The voltage of each channel can be set with a potentiometer individually. The board has an analogue and a TTL output and the option to be controlled remotely via USB.

2.4. Temperature Control

The NUV SiPM detector is sensitive in an energy range between approximately 50 and 550 keV, limited by the background and the energy absorbable in the scintillator. To shift this sensitivity to lower energies, the SiPM needs to be cooled down, since the dark count rate (DCR) depends on the overvoltage and the temperature. The reduction of the DCR coming from thermal noise brings the effective change in gain needed for lower energies. In addition to that, it is important to establish thermally stable conditions for a measurement since the breakdown voltage of the SiPM and, therefore, the gain of the system is temperature-dependent. To accomplish this, an in-house prototype cooling device similar to a cold finger was created. A cold finger is a device that cools an object by making thermal contact with the object that needs to be cooled. To allow heat to be transferred, it is necessary to connect the cold finger to a heat sink. In this case, the cold finger is constructed out of one copper spiral that is connected to the PCB below the SiPM. For measurements inside a cavity, the copper spirals are connected to a copper feedthrough, which ensures thermal contact with the outside. As a prototype of the coldfinger, a 1 L styrofoam box has been used. This setup made it possible to cool down the SiPM from room temperature to 0 °C and is displayed in the left part of Figure 2.12.

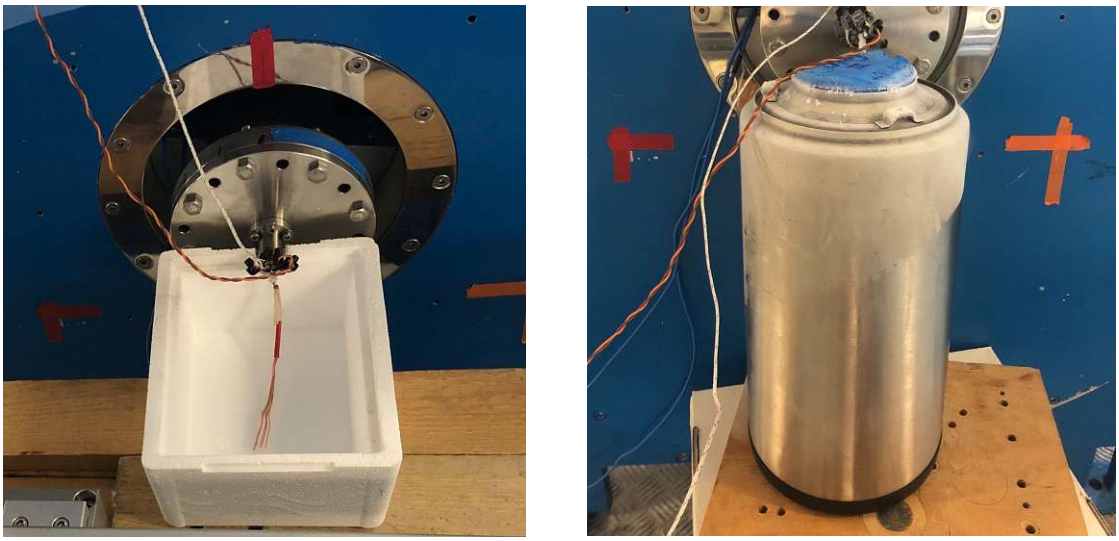

Figure 2.12.: Left: Styrofoam box used as a prototype of the cooling system. Right: 5 L dewar used for the cooled measurements performed within this thesis.

Due to the limited volume of the box, this setup restricted measurements to a

time of approximately 30 min after which the box had to be refilled. Since the refilling process includes an increase in temperature for the setup, this prototype was insufficient for real measurements. To increase the period with stable conditions, the styrofoam box was replaced by a 5 L dewar. Once filled with LN_2 and after a cooldown phase, the dewar makes it possible to have stable conditions at −6 °C for six hours. This improved the quality and the statistics of the recorded spectra significantly. The dewar used for the final cooling system can be seen in Figure 2.12.
Using a Peltier element would also have been possible, but it turns out that the thermal conductivity of the stainless steel alloy used in the vacuum chamber is too small to efficiently dissipate the heat from the Peltier element. As a result, the Peltier element cannot be used inside of the vacuum chamber.
Due to the limited duration of this work, only tests with the AdvanSiD NUV SiPM were possible at low temperatures. For future work, it is planned to test the temperature stability and decrease in the DCR with the Hamamatsu SiPM array.

2.5. Calibration Sources

To induce scintillation light, different radioactive sources have been used, as shown in Table 2.4. Some of these sources have been used to calibrate the detector to the energy range of incident particles. In this table, electrons are only mentioned for ^{109}Cd since all other sources are surrounded by epoxy, which fully absorbs the generated electrons. The sources have been placed directly on the scintillator for the measurements to minimize the distance that a particle has to travel before it interact with the scintillator. To measure electrons with the ^{109}Cd source, the setup needs to be in a vacuum.

Sample	$t_{1/2}$ [days]	Activity 2024 [kBq]	Peak Energy [keV]
^{241}Am	158 153	36.07	γ: 59.5409(1)
^{109}Cd	462.1(3)	5.3	γ: 88.0336(10) e^-: 62.520 84.2279 - 84.6826
^{133}Ba	3839	5.11	x-ray: 30-35 γ: 80.9979(11) 356.02
^{133}Ba	3839	19.27	x-ray: 30-35 γ: 80.9979(11) 356.02
^{152}Eu	4639	7.71	x-ray: 39-45 γ: 121.7817(3)
^{137}Cs	10 994	21.78	γ: 661.66

Table 2.4.: Overview of the most important properties of the calibration sources. Data of the peak energies is taken from [58–61].

3. Data Analysis and Results

In the analysis of the experimental data collected in this work, multiple Python scripts were written for the processing of the recorded datasets. The scripts take the acquired data as input and leverage the *pandas* library for effective management of the datasets [62]. The loaded data will then be processed further by normalizing, performing fits, and analyzing noise, depending on the type of data, originating from a pulse or a spectrum. The pulses will be analyzed based on their shape, considering different scintillators, bias currents, and readout methods, as well as their pre-trigger noise levels. Additionally, the influence of different readout methods on the shape of the spectrum will be discussed.

3.1. Fit Functions

For the pulses recorded as explained in Chapter 2 and spectra, different fit functions have been used to obtain all important parameters of the measurement. All fits have been performed using the *curve_fit* function from the *SciPy* submodule *scipy.optimize* [63].

Gaussian Fit

For the peaks of the spectra, a Gaussian function has been used to fit the data. This function was defined with the three free parameters that one can see in the following equation:

$$f(x) = a \cdot \exp\left[\frac{(x - x_0)^2}{2 \cdot \sigma^2}\right], \tag{3.1}$$

where a is the amplitude, x_0 a possible offset of the Gaussians center and σ a measure for the width of the Gaussian. This function is only used for monoenergetic peaks. But for some sources, two emission energies might be too close to each other, such that the energy resolution of the detection system can not resolve the single peaks anymore, and therefore, the spectrum consists of one single peak that consists of the sum of the two overlapping individual peaks. For this case, a fit of multiple Gaussian functions has been performed such that one can obtain information on the individual peak locations of the two merged peaks. The function of

this multi-Gaussian fit has been defined as follows:

$$f(x) = a_1 \cdot \exp\left[\frac{(x - x_{01})^2}{2 \cdot \sigma_1^2}\right] + a_2 \cdot \exp\left[\frac{(x - x_{02})^2}{2 \cdot \sigma_2^2}\right] \tag{3.2}$$

Tri-exponential Fit

A sum of three exponential functions has been used to fit the pulses obtained from the scintillation detection system (see Figure 2.1). These exponential functions correspond to the rise time and the two decay time components of the scintillator. As described in [44], one usually uses two falling components for the fit to accommodate for the short-lived and long-lived excitations that can be caused by an incident particle. This tri-exponential fit function has been defined as follows:

$$f(x) = A \cdot \left(\mathrm{e}^{-b_0 \cdot (x - x_0)} - \mathrm{e}^{-b_1 \cdot (x - x_1)}\right) + A \cdot \mathrm{e}^{-b_2 \cdot (x - x_2)}, \tag{3.3}$$

where A is the amplitude, b_i the decay constants and x_i a possible vertical offset.

3.1.1. Pulse Shape Parameters

The important parameters of pulses, produced after the absorption of radiation in a crystal in the setup schematically depicted in Figure 2.1, are defined as shown in Figure 3.1. The important parameters of a pulse are:

- rise time - defined as the duration the signal needs to increase from 10% to 90% of the pulse height
- decay time - defined as the time after which the pulse has returned to 1/e of its maximum value
- signal width - defined as the duration between the first and second signal crossings of 50% of the pulse height
- undershoot - defined as the occurrence of a signal exceeding the baseline on the falling edge

With the undershoot shown in the same figure, it is not purposeful to use the decay time in the analysis of the recorded pulses. The undershoot of the pulse is specific to the electronic board used for the measurements and cannot be changed.

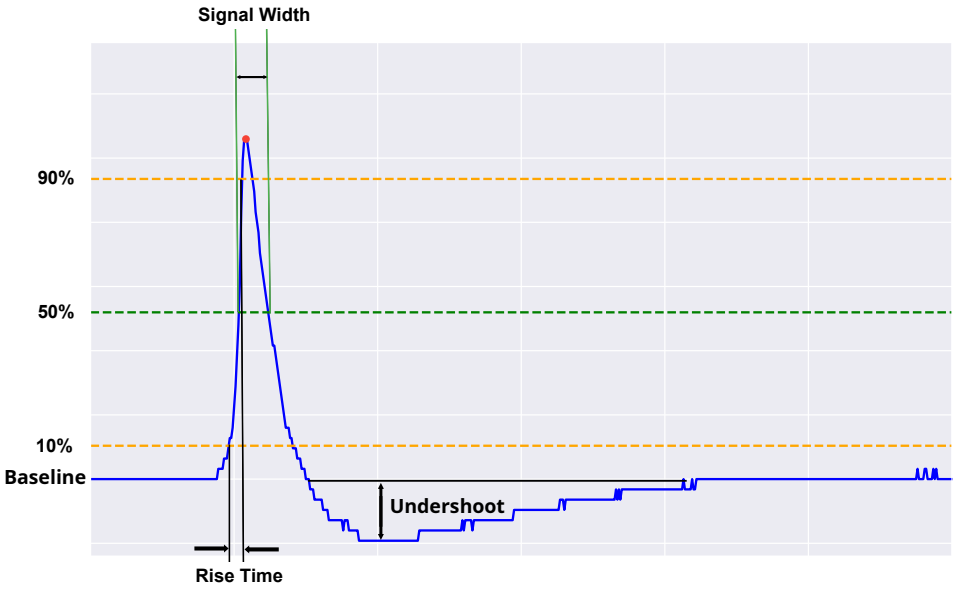

Figure 3.1.: Important quantities of the pulses. The baseline is set to the average value of the pre-trigger data. The rise time is defined as the duration the signal needs to increase from 10% to 90% of the pulse height. The decay time is defined as the time after which the pulse has returned to 1/e of its maximum value. The signal width is defined as the duration between the first and second signal crossings of 50% of the pulse height. The undershoot is defined as the occurrence of a signal exceeding the baseline on the falling edge. The undershoot of the pulse is specific to the electronic board used for the measurements and cannot be changed.

SNR

The SNR for the pre-trigger noise of the pulses recorded in this work has been defined as follows:

$$\mathrm{SNR} = \frac{\text{pulse height}}{\text{pre-trigger noise}} \tag{3.4}$$

3.2. Readout with Hamamatsu SiPM MPPC Array

The whole MPPC array consists of 16 individual SiPMs. To investigate possible deviations of these individual SiPMs in terms of gain, stability, and noise, 8 out of the 16 SiPMs have been measured under the same conditions with the developed setup. The SiPMs of the unit can be read out, or, by connecting the cathodes and annodes via a stripboard, grouped and read out collectively. For the discussions, the average of 128 pulses has been used to eliminate pre-trigger noise, reduce pile-up events, and diminish the effects of single pulses that are significantly smaller or larger. The important parameters of the pulses for the measurements are the rise time and the peak height.

3.2.1. Adapter-PCB

To power the individual SiPMs of the Hamamatsu array, an adapter PCB has been designed within the framework of this thesis. Figure 3.3 shows the connector on the backside of the SiPM array.

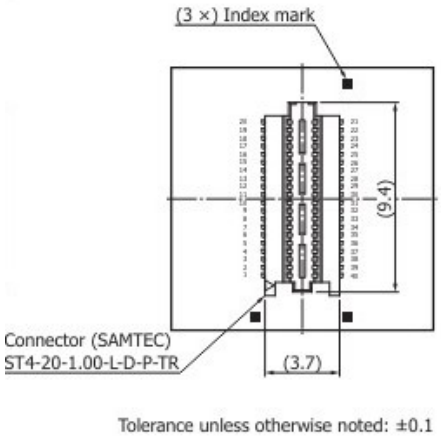

Figure 3.2.: Backside of the Hamamatsu MPPC array with the connector. Taken from [43].

The distance between anode and cathode on the connector itself is 0.4 mm. In order to have more space for the soldering and to increase the accessibility, the individual connections have been spread out as can be seen in the right part of Figure 3.3. The naming of the pads corresponds to the position of the SiPMs on the array (A1-D4) and the polarity (cathode (k), anode (a)).

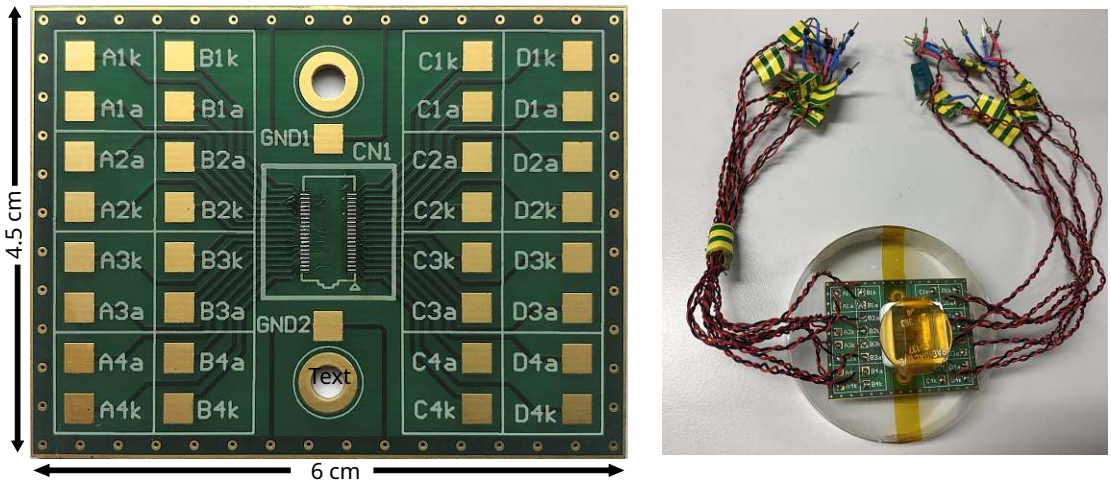

Figure 3.3.: Left: The in-house designed adapter connecting the array of 16 SiPMs to the power supply. Right: Connector with all 16 pairs of twisted cables soldered to it and the BC-408 plastic scintillator with a ^{137}Cs source on top of the scintillator

The adapter also has the option to be grounded via two channels and attached to a holder with the two screws used for grounding (GND1 and GND2). For the simultaneous readout of multiple SiPMs, the affected cathodes and anodes need to be connected in parallel.

3.2.2. Gain Stability

To check gain stability, for example for possible drifts due to various processes in the electronics, a series of 12 consecutive measurements over two days has been performed. On each day, six measurements in timesteps of one hour have been performed. The pulse height of these pulses has been extracted via a tri-exponential fit (Equation 3.3). The amplitudes of the recorded signal have been plotted against

time, which is shown in Figure 3.4. The measurements were performed with the Hamamatsu array (SiPM A1), a ^{133}Ba source (gammas with 81 - 356 keV), the BC408 plastic scintillator and 7.2 µA bias current. The error bars represent the standard deviation of the given pulse heights.

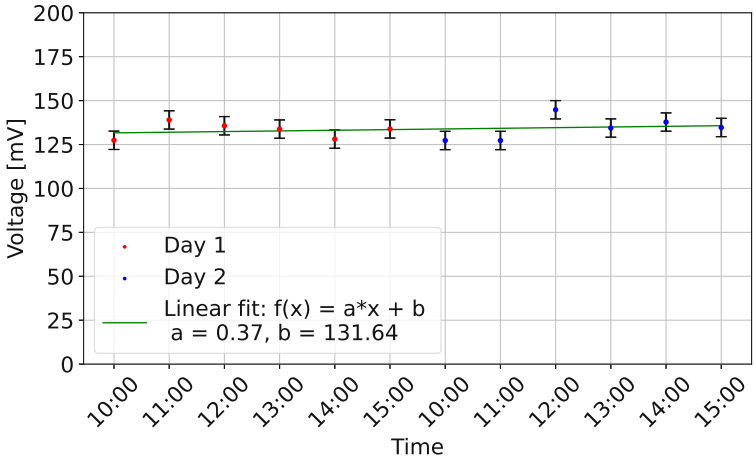

Figure 3.4.: pulse height of measurements performed in six timesteps of one hour over two days. The measurements were performed with the Hamamatsu array (SiPM A1), a ^{133}Ba source (gammas with 81 - 356 keV), the BC408 plastic scintillator and 7.2 µA bias current. The error bars represent the standard deviation of the given pulse heights. The plot shows a slight shift in gain by 0.37 mV h^{-1}. The average pulse height is 133.7 ± 5.2mV.

The plot shows a slight shift in gain by 0.37 mV h^{-1}. The exact data of the measurements can be seen in Table 3.1. The standard deviation of 5.2 mV means a relative deviation of 3.9% of the pulse height. The average pulse height is 133.7 ± 5.2mV. This deviation is acceptable given the ambient temperature fluctuations of $\Delta T = 2\,°C$ and the temperature coefficient of the breakdown voltage of $\Delta T(V_{op}) = 54\,\text{mV}\,°\text{C}^{-1}$.

Measurement	Pulse Height [mV]
1	127.4
2	139.0
3	135.7
4	133.8
5	128.1
6	133.9
7	127.3
8	127.3
9	144.8
10	134.4
11	137.8
12	134.7
$\bar{x}$	133.7
σ	5.2

Table 3.1.: Data extracted from the time-series measurement with the Hamamatsu array (SiPM A1), a ^{133}Ba source (gammas with 81 - 356 keV), BC-408 and 7.2 µA. Measurements 1-6 were performed on day one, each one hour apart, and measurements 7-12 on day two.

3.2.3. Individual Readout

Each SiPM out of the 16 in the array was biased individually to see differences in gain and noise between different SiPMs on the same array. In addition, different scintillators have been used to show the differences in their rise time and the detector response. All fits for the pulses were performed using the tri-exponential function (Eq. 3.3).As one can see, for example, in Figure 3.6, which shows the average of 128 pulses recorded with a BC-408 plastic scintillator, the readout electronics produce an undershoot on the falling side of the pulse, which increases the time needed for the pulse to relax back to the baseline. To fit a function to this pulse, the second part of Eq. 3.3 was given a new amplitude B. To increase SNR and to average the pulse height, for all plots of pulses in this section, the average of 128 pulses has been used.

Effect of various Scintillators on Signal Output

The amount of scintillation light after the scintillator absorbs a particle is characteristic of the scintillator material. To analyze these differences in the SiPM output a series of measurements has been performed. For achieving comparable results, all measurements have been performed with the same SiPM (A1, see Figure 3.5),

the same bias current (7.2 µA), the same ^{137}Cs source and under ambient temperature and pressure in the PERC-laboratory of the Atominstitut of the Technische Universität Wien. The trigger threshold has been set to 40 mV for all measure-

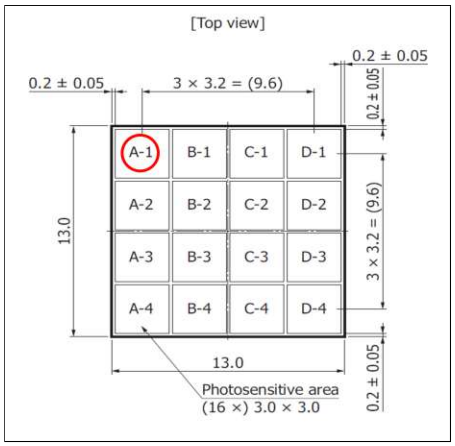

Figure 3.5.: The red circle highlights the position on the Hamamatsu array of the SiPM used for the measurements with different scintillators. The scheme of the array was taken from the datasheet [43].

ments. The rise time of $\tau_r = 9.18$ ns for the BC-408 scintillator is by a factor of 4.5 lower than the rise time of BGO ($\tau_r = 41.68$ ns), which is shown in Figure 3.7. This is in accordance with the scintillation decay time constants of these crystals.

The pulses from the BGO crystal are $\approx$ 75 mV (38 %) lower than the pulses coming from the plastic scintillator BC-408. The third scintillator that was measured was a YSO crystal. The measured pulse heights are for YSO 1094.1 mV, for BGO 121.4 mV and for BC-408 201.4 mV. From this, one can conclude that the brightness of the YSO crystal is by a factor of 5 higher than the brightness of BC-408. Also, the BGO crystal shows signs of radiation damage from earlier usage, causing it to be less bright than in undamaged conditions. Another factor for this is the geometry of the scintillator. The diameter of the base area of the cylinder is 5 mm which enables one to place it directly above one single SiPM with minor overlap to the surrounding ones. While the other scintillators lose part of the induced light to the whole array, the YSO scintillator and the Teflon tape in which it is wrapped guide the scintillation light towards the measured SiPM. At the same time, the undershoot of the pulse is also more prominent in the YSO pulse, as it grows with the pulse height. In addition, the ^{137}Cs source emits gammas at 662 keV, which is too high to be fully absorbed in BC-408, causing a lower light yield.

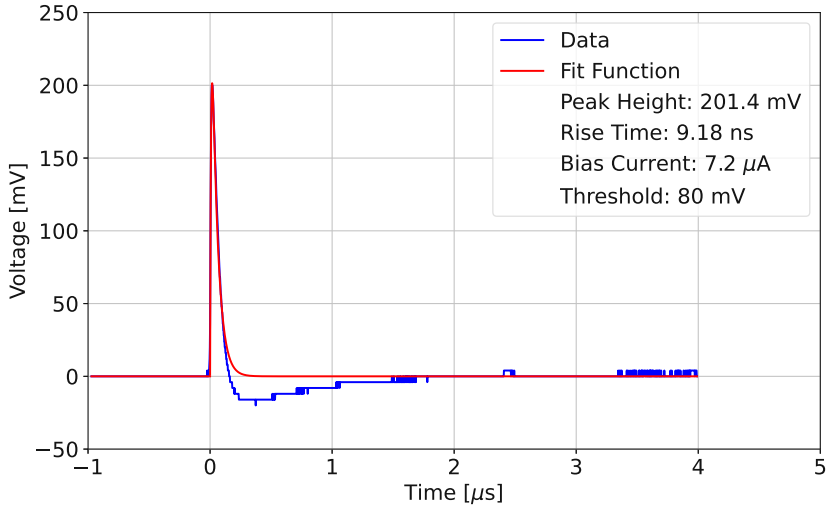

Figure 3.6.: Averaged pulse recorded with the SiPM A1 of the Hamamatsu array at 7.2 µA. For this measurement, a ^{137}Cs source (662 keV gammas) was used at room temperature together with a BC-408 plastic scintillator.

For better comparability, the data obtained from the fits is listed in the following Table 3.2:

	Measured Rise Time τ_r [ns]	Scintillation Decay Time [ns]	Pulse Height [mV]
BC-408	9.18	2.4	201.4
BGO	41.68	300	124.4
YSO	34.83	50-70	1084.1

Table 3.2.: Data for the different scintillators obtained from the fit functions. Literature values taken from [46–49]

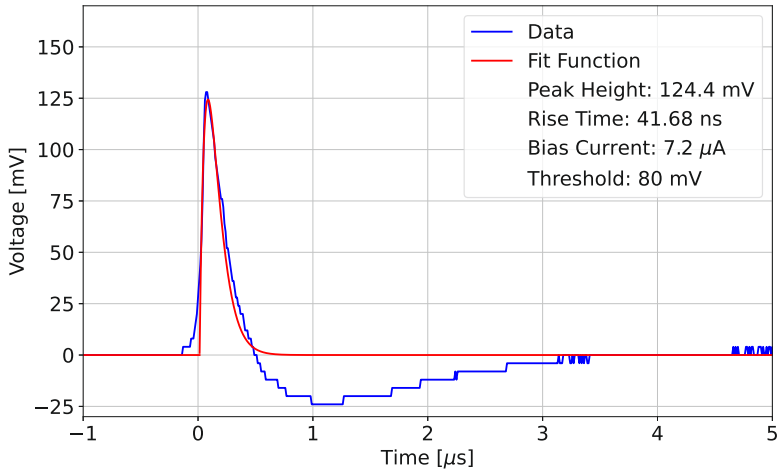

Figure 3.7.: Averaged pulse recorded with the SiPM A1 of the Hamamatsu array at 7.2 µA bias current. For this measurement, a ^{137}Cs source (662 keV gammas) was used at room temperature together with a BGO scintillator.

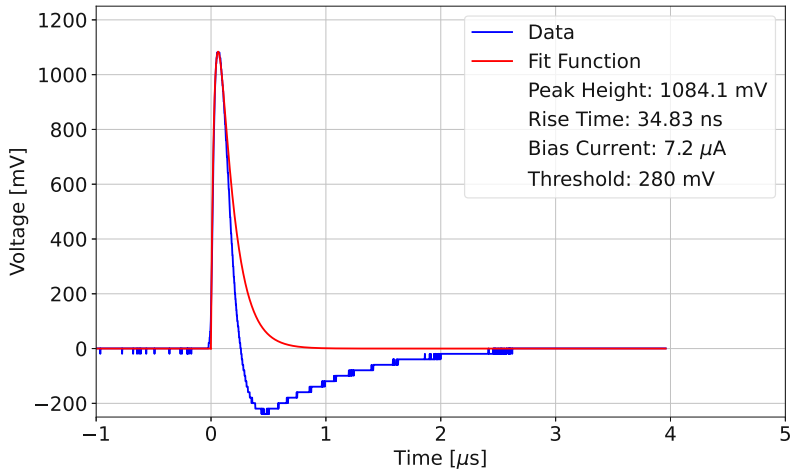

Figure 3.8.: Averaged pulse recorded with the SiPM A1 of the Hamamatsu array at 7.2 µA bias current. For this measurement, a ^{137}Cs source (662 keV gammas) was used at room temperature together with a YSO scintillator.

Optimum Bias Current

A change in the bias current/voltage supplied to the SiPM causes an effective change in gain. To investigate the influence of this change in the amplitude of the pulse, measurements with different bias currents have been performed with the SiPM at position A1 and the BGO crystal. The bias current and the corresponding bias voltage used for the measurements can be seen in Table 3.3. With the amplifying board (Figure 2.11), one can only directly measure the bias current, a 8 MΩ resistor has been connected to the input side of the board to calculate the values of the bias voltage from the current using *Ohm's Law*. The measurements have been performed with steps of 0.4 µA, starting at 6.4 µA and reaching up to 8 µA. However, the noise in the measurements with 6.2 µA and 8 µA was already dominating the signal and these measurements have not been taken into account for the evaluation.

The plots of the averaged pulses of these two measurements are shown in the appendix A.1. The pulse with the lowest bias current of 6.8 µA (Figure 3.9) shows the lowest amplitude with a height of 47.0 mV. The fits (red lines) in Figures 3.10 (7.2 µA) and 3.11 (7.6 µA) indicate that the pulse height keeps rising with increasing bias current. The measured pulse rise time remains constant with increasing bias current (average: $\tau_r = 43.42 \pm 0.88$ns). All the fitted parameters can be found in Table 3.3:

I_{Bias}	V_{Bias}	Rise Time τ_r	Pulse Height
6.8 µA	54.4 V	44.16 ns	47.0 mV
7.2 µA	57.6 V	42.18 ns	121.2 mV
7.6 µA	60.8 V	43.91 ns	143.2 mV

Table 3.3.: Parameters extracted from the fits of the pulses measured with different bias currents and the BGO crystal. All measurements have been performed with the SiPM at position A1 and the ^{137}Cs gauge source.

Figure 3.12 shows the pulse height of the pulses plotted against the bias current they were recorded with. It visualizes that the increase in pulse height is by about a factor of 3 for the step from 6.8 µA to 7.2 µA. When increasing the bias current further by another 0.4 µA, the pulse height grows by a factor of 1.2. The observed increase in the pulse height is not the only effect induced by the higher bias current. As the overvoltage rises, so does the DCR of the SiPM. An analysis of the noise and the background of the system will be done in section 3.2.5.

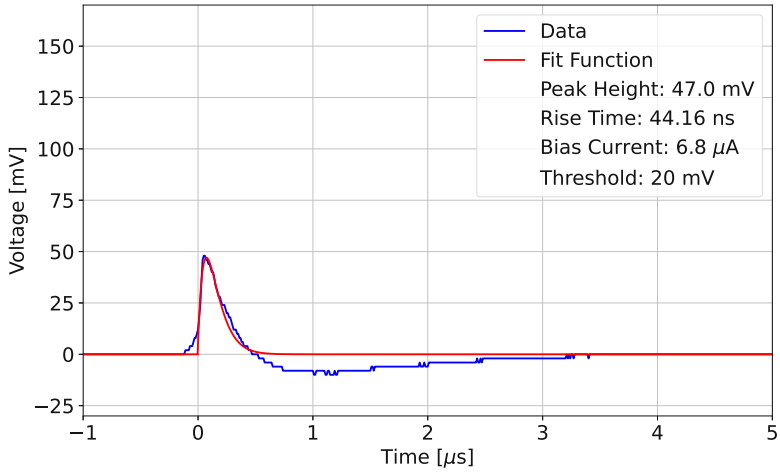

Figure 3.9.: Averaged pulse recorded with SiPM A1 of the Hamamatsu array using a ^{137}Cs source (662 keV gammas) at room temperature and a BGO crystal. The measurement was performed using 6.8 µA bias current.

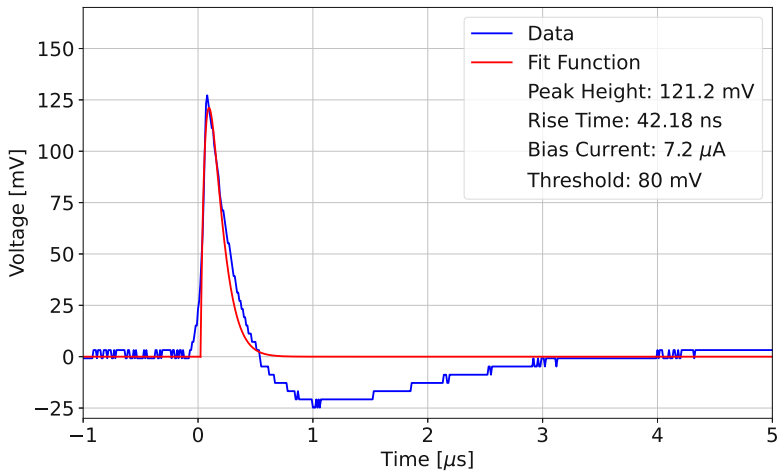

Figure 3.10.: Averaged pulse recorded with SiPM A1 of the Hamamatsu array using a ^{137}Cs source (662 keV gammas) at room temperature and a BGO crystal. The measurement was performed using 7.2 µA bias current.

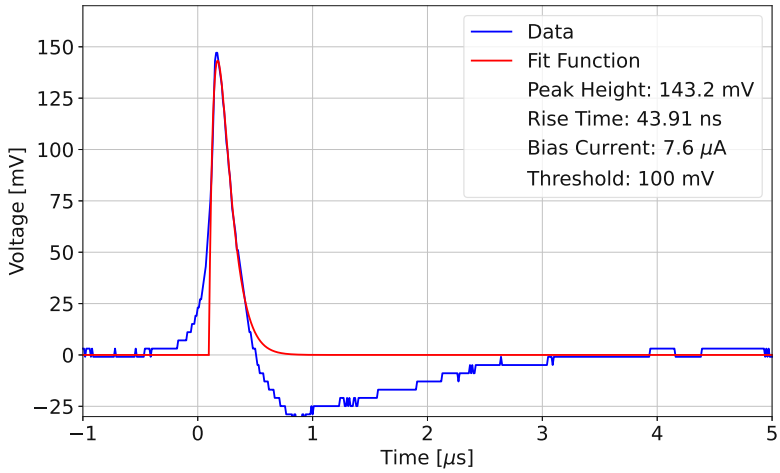

Figure 3.11.: Averaged pulse recorded with SiPM A1 of the Hamamatsu array using a ^{137}Cs source (662 keV gammas) at room temperature and a BGO crystal. The measurement was performed using 7.6 µA bias current.

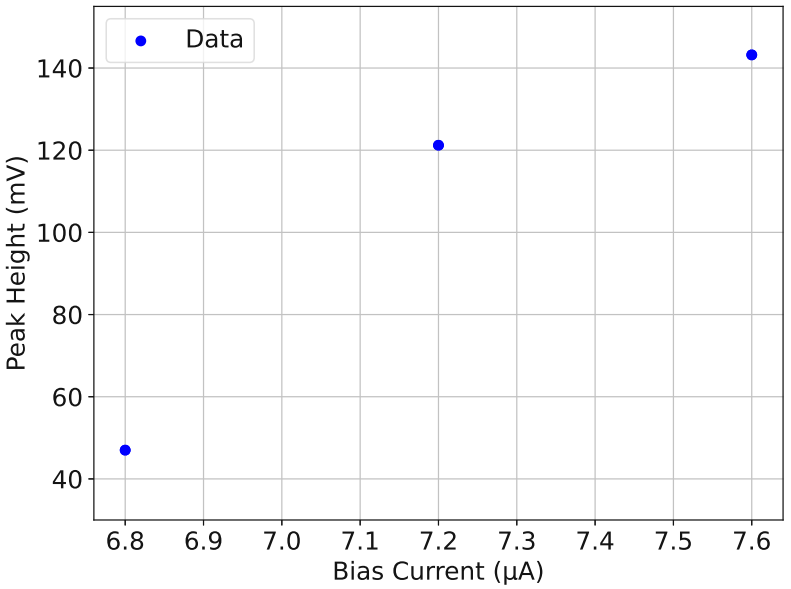

Figure 3.12.: Pulse height plotted against the bias current from the measurements with SiPM A1 of the Hamamatsu array using a ^{137}Cs source (662 keV gammas) at room temperature and a BGO crystal.

Individual SiPMs with BC-408

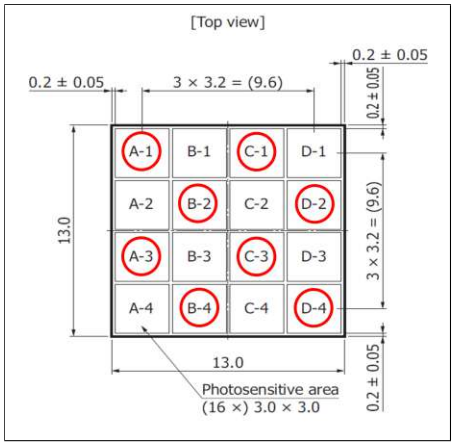

Figure 3.13.: The red circles highlight the positions on the array of the SiPMs used for the measurements. The scheme of the array was taken from the datasheet [43].

All measurements have been performed under the same conditions (see Figure 2.1). The same channel of the power supply was used while keeping the bias current stable at 7.2 µA. The ^{137}Cs source (662 keV gammas) described in Section 2.5 has been used. The pattern of the SiPMs selected for measurements can be seen in Figure 3.13. The selected SiPMs spread evenly across the whole array to maximize the overall tested area of the array. The scintillator chosen for these measurements was BC-408 since a similar plastic scintillator (BC-404) will be used at PERC as a main and backscattering detector. BC-404 differs in the emission spectrum (peak at 408 nm) and the hydrogen content, but has a decay time constant of 1.8 ns in the same order as BC-408 (2.4 ns). The values for BC-408 are taken from [64], where additional information on the plastic scintillator is given.
The plot in Figure 3.14 represents one of the eight measurements done within this series, all of them containing an average of 128 pulses.

All the other plots of the individual measurements can be found in Appendix A.3. In addition to the obtained data, the mean $\bar{x}$ and the standard deviation σ have been calculated. δ is the change in the rise time (τ_r) relative to the mean rise time in percent. The extracted data from all individual SiPMs is displayed in Table 3.4:

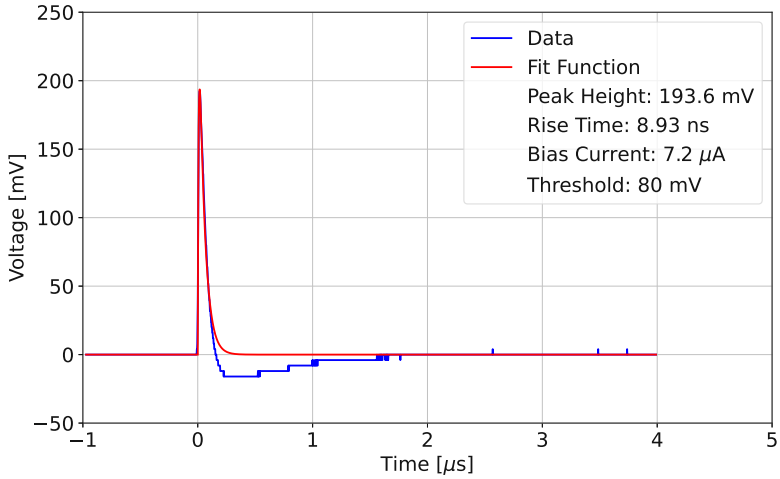

Figure 3.14.: Representative plot of the averaged pulse recorded from a ^{137}Cs source (662 keV gammas) at room temperature using a BC-408 plastic scintillator at SiPM A3. A measurement like this one has been performed for 8 out of the 16 SiPMs of the Hamamatsu array. The measurement was performed using 7.2 µA bias current.

Position	Rise Time [ns] τ_r	Pulse Height [mV]	δ [%]	Signal Width [ns]
A1	9.18	201.4	-0.97	55.4
A3	8.63	241.3	-6.91	61.7
B2	8.93	193.6	-3.66	55.5
B4	8.78	257.2	-5.29	61.1
C1	9.97	238.1	5.29	58.0
C3	10.02	229.8	8.09	60.8
D2	9.53	216.4	2.80	55.8
D4	9.08	235.5	-2.04	58.3
$\bar{x}$	9.27	226.7		58.3
σ	0.49	20.0		2.5

Table 3.4.: Parameters collected from 8 out of 16 SiPMs of the Hamamatsu array at 7.2 µA with the BC-408 scintillator and the ^{137}Cs source (662 keV gammas). In addition to the obtained data, the mean $\bar{x}$ and the standard deviation σ have been calculated. δ is the change in the rise time (τ_r) relative to the mean rise time in percent. The average rise time is 9.27 ± 0.49ns and the average pulse height 226.7 ± 20.0mV.

The calculated standard deviation shows that the individual SiPM, even after averaging over 128 pulses, still shows a deviation in their pulse height up to ±8.8 %. The rise time comes with a σ of ±5.1 %. This non-uniformity shows that if one wants to read out the SiPMs individually, each SiPM has to be characterized. The backscattering detector of PERC will consist of 10 × 10 Hamamatsu units. For these 1600 individual SiPMs, one would need to perform an energy calibration to increase the SNR of the final backscattered electron spectrum.

3.2.4. Collective Readout

By changing the readout electronics one can achieve a collective readout of multiple SiPMs at the same time. To be more specific, one has to connect the anodes and cathodes of the SiPMs concerned in parallel for this readout method. This reduces the amount of cables on the readout side by a factor of 4 and lowers the amount of individual calibrations that would need to be performed for the backscattering detector. This has been done in two different patterns. First, the SiPMs were grouped into four groups of four neighbouring elements, as one can see in Figure 3.15.

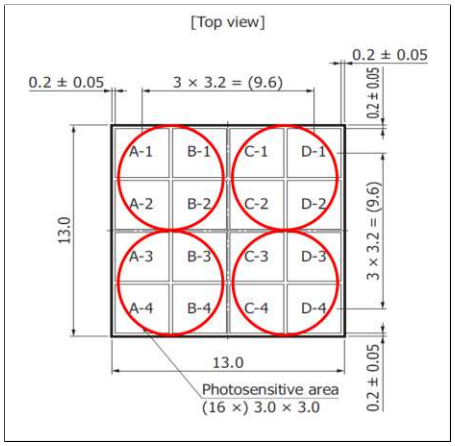

Figure 3.15.: The red circles highlight the positions on the array of the SiPMs used for the measurements. The groups were named after the SiPMs; they consist of AB12, AB34, CD12, and CD34. The scheme of the array was taken from the datasheet [43].

After measuring those 4 areas, the whole unit of 16 SiPMs is read out as one detector to be able to see the effect of this enlargement on the pulses. All these measurements have been performed using the BC-408 plastic scintillator the same channel of the power supply, set to the same supplied voltage as for the measurement with 7.2 µA. As a source, the stronger ^{133}Ba source (gammas with 81

- 356 keV) listed in Table 2.4 has been used. To give a comparison, the average of 128 pulses from the same source and with the same settings has been recorded with the SiPM at location A1.

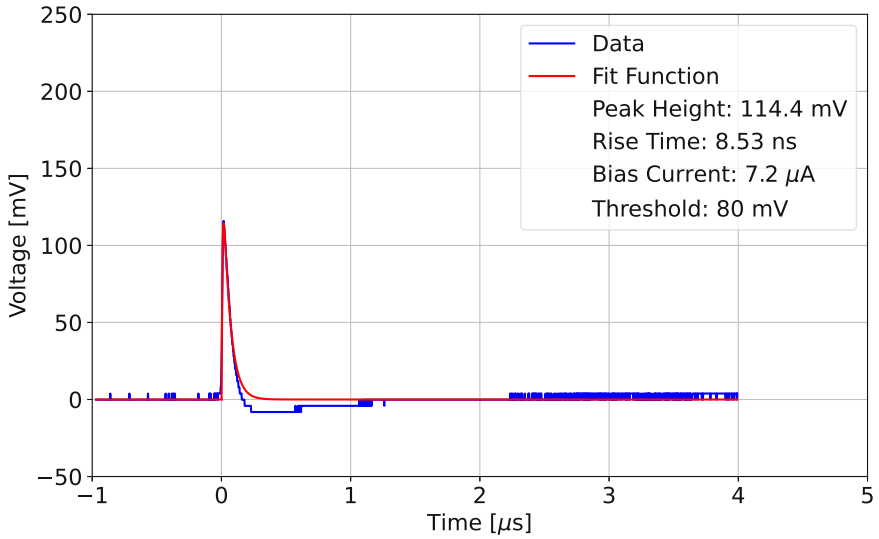

Figure 3.16.: Averaged pulse - recorded with a single SiPM (A1) of the Hamamatsu array - from a ^{133}Ba source (gammas with 81 - 356 keV) at room temperature using a BC-408 plastic scintillator. The measurement was performed using 7.2 µA bias current.

The undershoot of the pulse is more prominent compared to the individual readout SiPM. The same tendency can be seen in Figure 3.18, which shows the pulse coming from the whole unit read out simultaneously. Merging all 16 SiPMs increases the rise time by an overall factor of 4. To compare these two setups, one needs the data of the whole unit, which means all 4 groups of SiPMs and more than one measurement of the unit itself.
The fit results of all these measurements can be found in Table 3.5. Figure 3.16 shows that the rise time of SiPM A1 ($\tau_r = 8.53$ ns) is similar to the data found in Table 3.4 (average rise time $\bar{\tau_r} = 9.27 \pm 0.49$ ns), which is coming from the individual readout of eight different SiPMs with the same BC-408 plastic scintillator. The pulse height of 114.4 mV is by about a factor of 2 lower than the average of the individual measurements (226.7 mV) with ^{137}Cs (gammas with 662 keV). Since the recorded pulses are coming from the ^{133}Ba source (81 - 356 keV gammas), this factor of 2 appears to be in agreement with Birks' Law (Equation 2.1), which states a proportionality between the energy absorbed by the scintillator and the light yield.

The collective read out of the 4 SiPMs A1, A2, B1, and B2, as shown in Figure 3.17, produces a higher pulse and increases the rise time of the pulse by a factor of 2. By reading out the whole array as one unit, the rise time and the pulse height continue to increase, as shown in Figure 3.18. Compared to the collective measurement of 4 SiPMs, the average rise time of the unit ($\bar{\tau} = 39.04\,\text{ns}$) is by a factor of 2 higher and the average pulse height (317.4 mV) increased by a factor of 1.25. If the values are compared to the individual measurements, the rise time grew by about a factor of 4.5 and the pulse height by about a factor of 3. The time of flight (ToF) for backscatter events at PERC is about 50 ns. This means that the prolongation coming with the readout in groups of 4 is acceptable since the rise time is still below the ToF. For the whole unit, one rise time of the three measurements is already above 50 ns, which is not ideal since it might cause missed identifications of backscattering events. However, the sample size of three measurements is too small to conclude that the pulses from the unit are too slow for this purpose.

Position	Rise Time τ_r [ns]	Pulse Height [mV]	δ [%]
1 SiPM			
A1	8.34	109.9	-1.30
A1	8.53	114.4	0.95
A1	8.49	109.1	0.47
$\bar{x}$	8.45	111.1	
4 SiPMs			
AB12	18.26	249.6	-0.54
AB34	18.76	241.2	2.18
CD12	18.16	249.6	-1.09
CD34	18.36	267.4	0.00
$\bar{x}$	18.36	252.0	
16 SiPMs			
Whole	31.76	314.6	-18.65
Whole	51.61	322.5	32.20
Whole	33.74	315.0	-13.58
$\bar{x}$	39.04	317.4	

Table 3.5.: Data collected from the Hamamatsu array with different read-out methods: individual, in groups of four SiPMs, and as a whole array. Pulses originate from the ^{133}Ba source (gammas with 81 - 356 keV) and the BC-408 scintillators measured with 7.2 µA. δ is the change in the rise time (τ_r) relative to the mean rise time in percent.

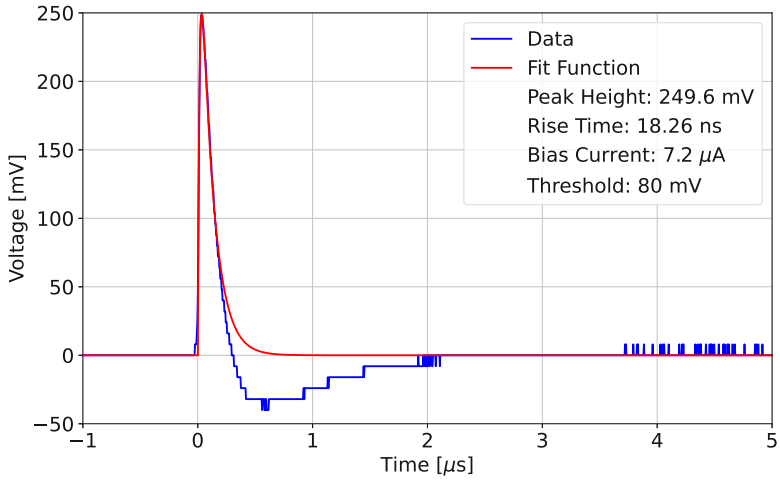

Figure 3.17.: Averaged pulse - recorded with 4 collectively read out SiPMs (A1, A2, B1, B2) of the Hamamatsu array - from a ^{133}Ba source (gammas with 81 - 356 keV) at room temperature using a BC-408 plastic scintillator. The measurement was performed using 7.2 µA bias current. Compared to the individual measurement, this pulse has a visibly increased rise time (by approximately a factor of 2).

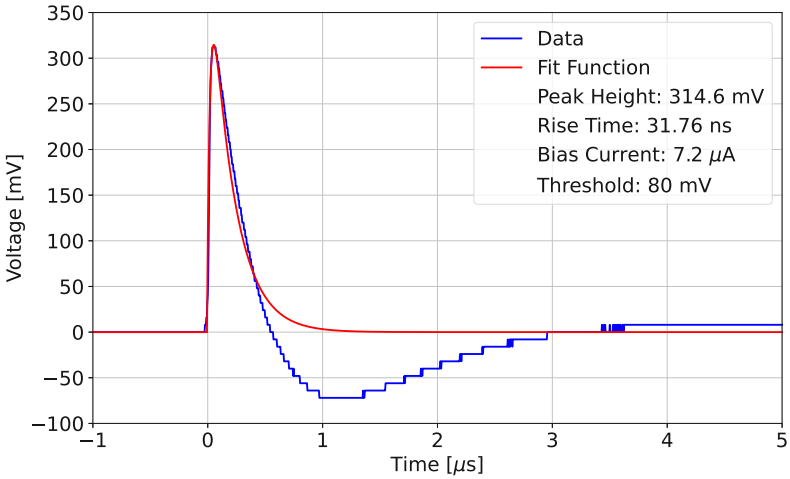

Figure 3.18.: Averaged pulse - recorded with the whole Hamamatsu array (16 SiPMs) read out collectively - from a ^{133}Ba source (gammas with 81 - 356 keV) at room temperature using a BC-408 plastic scintillator. The measurement was performed using 7.2 µA bias current. The rise time has again increased with the amount of connected SiPMs.

3.2.5. Pre-Trigger Noise

Many parameters can lead to an increase in the noise of the measured data. Examples of noise sources are:

- Temperature
- Readout electronics (cables, power supply, amplifiers, ADCs, ...)
- Readout method (individual, collective)
- External sources of pile-up events
- Bias voltage (overvoltage), DCR

To reduce the pick-up noise of the cables, a twisted pair of cables was used to connect the amplifying board to the ADC (*Analog Digital Converter*). The length of this twisted pair can also influence the SNR (*Signal to Noise Ratio*), which is why there has been performed a series of measurements with different cable lengths in Section 3.2.5. Another aspect is the gain change due to a change in bias voltage or individual readout in comparison to the collective readout in terms of noise. To check the level of noise one can take the data of a single pulse from the time before the pulse starts to rise, also referred to as pre-trigger region. This has been defined as 1/5 of the total pulse duration since this area does not include a signal in all pulses. A histogram was created that counts the amount of existing voltages in the pre-trigger region. The binning of this histogram is calculated from the difference between the highest and lowest noise values and the minimum voltage steps in the region. To obtain a numerical value for the range of this noise, a Gaussian function, Eq. 3.2, is used to fit the histogram.

The σ is then calculated from the FWHM extracted from the Gaussian function and used to evaluate the quality of the data. To be able to compare the results, the histogram has been normalized to 1. The noise level of SiPM A1 measured with 7.2 µA lies at about 6.6 mV. Since the pulse had a height of 241 mV, one obtains an SNR (see Eq. 3.4) of about 16, which means the signal is clearly distinguishable from the background. Figure 3.19 shows a single and an averaged pulse recorded with SiPM A1 of the Hamamatsu array at 7.2 µA coming from the ^{137}Cs source (662 keV gammas) and the BGO scintillator. It demonstrates the effect of the averaging on the pulse shape and the pre-trigger noise. The single pulse has a pile-up event with a height of $\approx$ 25 mV in the pre-trigger and shows an average noise of 6.6 mV, while the pre-trigger region of the averaged pulse is flat and shows no pile-up event. Therefore, averaged pulses were used for the discussions on the pulseshape.

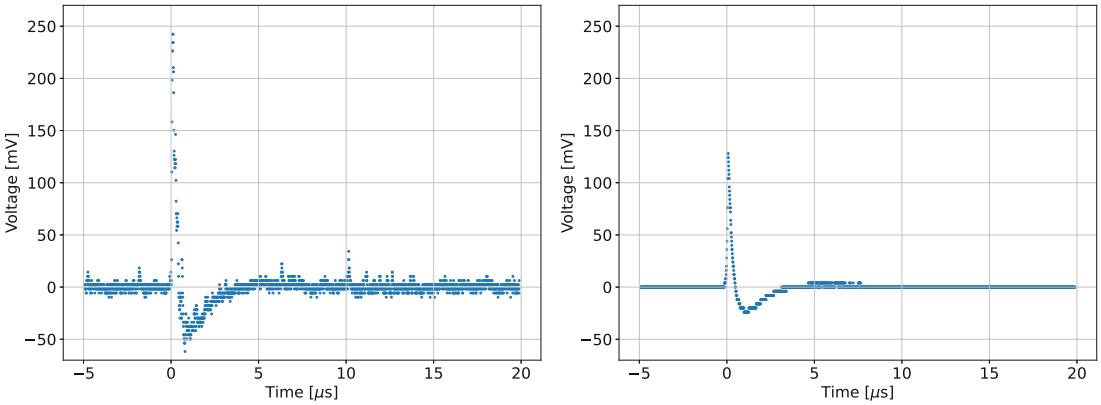

Figure 3.19.: Left: Single pulse recorded with SiPM A1 of the Hamamatsu array at 7.2 µA coming from the ^{137}Cs source (662 keV gammas) and the BGO scintillator. The pre-trigger region, defined as 1/5 of the total pulse duration, has been used to create a histogram of the baseline noise. Right: averaged pulse recorded with the same parameters and conditions.

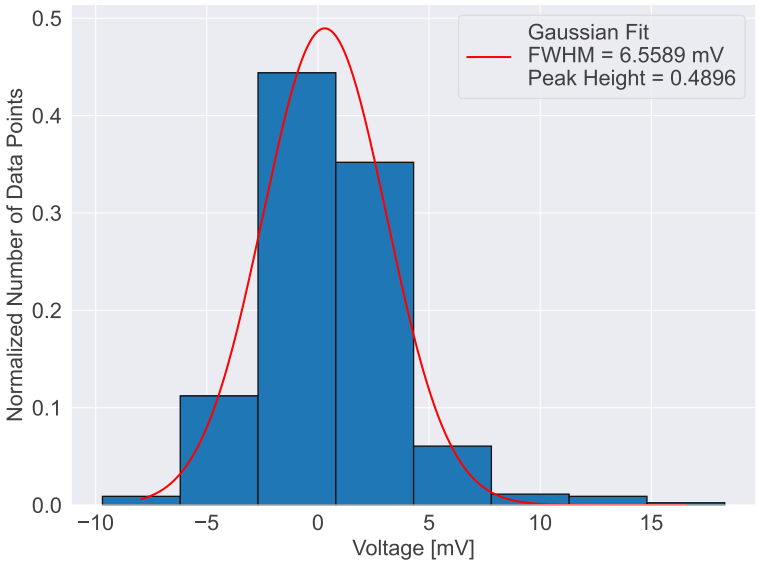

Figure 3.20.: Histogram created from the pre-trigger region of the data coming from a single pulse. The pulse was created with the SiPM A1 of the Hamamatsu array at 7.2 µA, the ^{137}Cs source (662 keV gammas) and the BGO scintillator. The red line is the Gaussian fit used to determine the FWHM and the peak height. The noise level is of the order of 6.6 mV.

Effect of the Bias Current on SNR

The first parameter to be checked for its influence on SNR is the bias current. The increase in the pulse height usually comes with an increase in noise. The data extracted from the Gaussian fit is displayed in the following Table 3.6: The data

I_{bias} [µA]	σ [mV]	SNR
6.8	1.79	41.94
7.2	2.79	86.93
7.6	3.38	44.82

Table 3.6.: Noise collected from the pre-trigger region of single pulses recorded with a ^{137}Cs source (662 keV gammas) the BGO scintillator and SiPM A1 of the Hamamatsu array at different bias currents.

coming from the measurement with 7.2 µA is already fitted in Figure 3.20. For the measurements with 6.8 µA and 7.6 µA the histogram is shown in the Figure 3.21. The histogram of the measurement with 7.6 µA is asymmetric compared to the other plots, which is caused by a small pile-up event in the pre-trigger region. This is not affecting the fit due to the weights set for the fit.

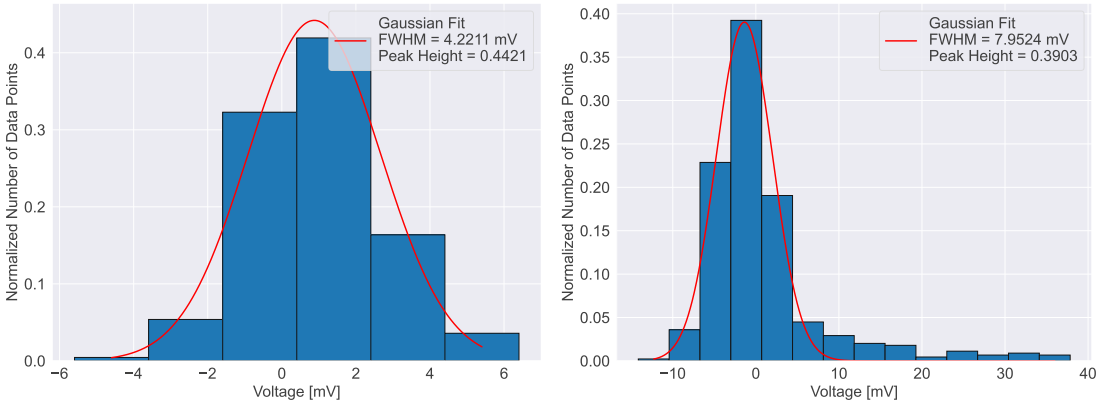

Figure 3.21.: Histograms created from the pre-trigger region of the data coming from a single pulse. The red line is the Gaussian fit used to determine the FWHM and the peak height. Both pulses were measured with the BGO scintillator, with SiPM A1, and with the ^{137}Cs source (662 keV gammas). Left: 6.8 µA Right: 7.6 µA. The longer tail in the right histogram is due to a small pile-up event in the pre-trigger region.

The measurement with the lowest bias current (6.8 µA) shows also the lowest noise level of 1.79 mV. Increasing the bias current to 7.2 µA increased the noise

level by a factor of 1.5 to 2.79 mV. At 7.6 µA the noise level has reached 3.38 mV, which is a factor of 1.9 higher compared to the lowest value. This means that the noise increases along with the bias current, which is due to the increase in the dark count rate of the SiPM at higher overvoltage. The best SNR was measured with 7.2 µA with a value of about 87. This is by a factor of 2 better than the other measurements with different bias currents. As shown by Figure 3.12, the step from 6.8 µA increased the pulse height by a factor of 3 while increased only by a factor of 1.2 from 7.2 µA to 7.6 µA. The noise level only increased by a factor of 1.5 from 6.8 µA to 7.2 µA, which causes the good SNR for the 7.2 µA measurement. The BGO crystal has been chosen randomly for this measurement since the purpose was to describe the influence of the bias current on the SNR, which is independent of the crystal.

Cable Length

The cables connecting the SiPM to the amplifying board have a length of 25 cm and are always of the same length for all measurements. But the cables connecting the amplifying board were measured for 190 cm and 75 cm. All these cables were twisted and of the same type. A series of measurements has been performed across the whole array (8 SiPMs in the same pattern as in Figure 3.13) with 7.2 µA using a ^{137}Cs source (662 keV gammas) and the BC-408 scintillator. The σ values for the single measurements and the average of the array can be seen in Table 3.6:

SiPM Position	Short (75cm)	long (190cm)
	σ [mV]	σ [mV]
A1	1.43	1.29
A3	1.50	1.28
B2	1.26	1.25
B4	1.44	1.23
C1	1.33	1.29
C3	1.29	1.38
D2	1.33	1.22
D4	1.13	1.45
$\bar{x}$	1.34	1.30
σ	0.11	0.07

Table 3.7.: Noise level for different cable lengths for the same detection setup (SiPM A1 of the Hamamatsu array, 7.2 µA, ^{137}Cs source (662 keV gammas)). The σ has been calculated by fitting a Gaussian to the noise of the pre-trigger region.

The average noise level of the 75 cm cable lies at 1.34 ± 0.11 mV. Using a cable length of 190 cm produced an average noise level of 1.30 ± 0.07 mV, which is of the same order as with the shorter cables. Therefore, twisted pairs of cables can be used up to 1.9 m without an increase in noise. The differences between the individual channels are statistical. The plots of the individual channels can be found in Appendix B.1.

Individual and collective Readout on SNR

In Section 3.2.4 it was shown that individual SiPMs might differ by about 10%. The collective readout prolonged the pulses by a factor of 2 (for 4 SiPMs) and by a factor of 4 (for 16 SiPMs). Therefore, the same evaluation of the pre-trigger region has been performed for single pulses of the collective readout. Selected plots of the individual read-out, the read-out in groups of 4, and the read-out of the whole array as one unit can be seen in Figure 3.22.
The σ increases with the amount of SiPMs read out simultaneously, but the height of the pulse increases as well. The averaged values of the pulse height obtained in Section 3.2.4 were 111.1 mV for the individual readout, 252.0 mV for the groups of 4 SiPMs and 317.4 mV for the 16 SiPM-unit. The pre-trigger noise is higher, but for the SNR, one needs to consider the relative noise height compared to the pulse height. The data collected from all the measurements performed for this section are summarized in Table 3.8. The SNR becomes better along with the number of channels read out simultaneously. The groups of 4 SiPMs have an average SNR that is by a factor of 1.4 higher than the individual readout and the unit of 16 SiPMs shows an increase in SNR by a factor of 1.8 compared to the individual readout. At the same time the rise time of the pulses increases by a factor of 2 from the individual ($\bar{\tau}_r = 8.4$ ns) to the collective readout of 4 SiPMs ($\bar{\tau}_r = 18.4$ ns) and by about another factor of 2 from groups of 4 to the whole unit ($\bar{\tau}_r = 39.0$ ns). So the pulse duration is longer, but 39.0 ns is still acceptable and the SNR of 32.2 was measured with this readout method. The crystal with the best SNR was YSO, since the SNR depends on the pulse height and YSO was the brightest crystal.

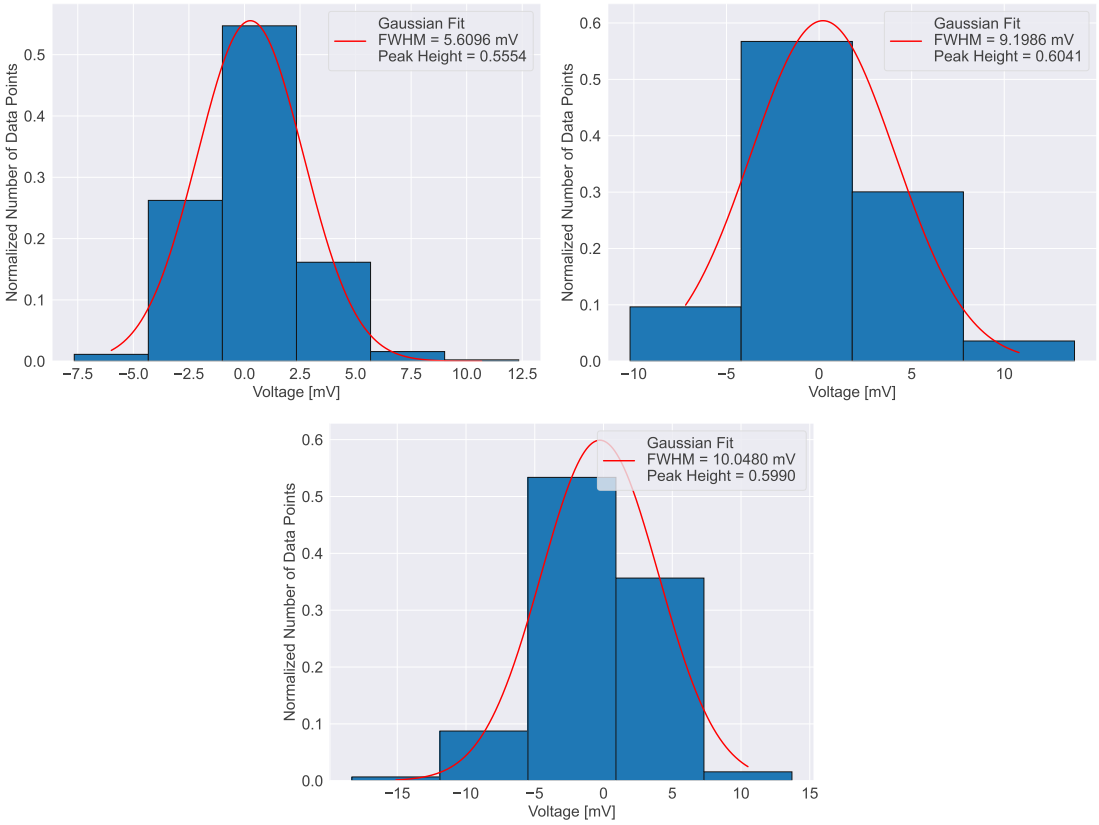

Figure 3.22.: Histograms created from the pre-trigger region of the data coming from a single pulse. The red line is the Gaussian fit used to determine the σ and the peak height. All were recorded using a ^{133}Ba source (gammas with 81 - 356 keV) and the same bias voltage, the BC-408 scintillator and the Hamamatsu array. Top-Left: single SiPM, Top-Right: four merged SiPMs (AB12), Bottom: Whole unit of 16 SiPMs read out as one

SiPMs	σ [mV]	SNR
1 SiPM		
A1	2.38	46.1
A2	2.78	39.4
B1	2.68	40.5
B2	2.67	41.9
$\bar{x}$	2.63	41.9
4 SiPMs		
AB12	4.43	56.0
AB34	3.91	65.6
CD12	4.55	54.9
CD34	4.49	56.0
$\bar{x}$	4.34	58.2
16 SiPMs		
Meas. 1	4.01	78.5
Meas. 2	4.11	76.1
Meas. 3	4.27	74.2
$\bar{x}$	4.13	76.1

Table 3.8.: Data collected from the different read-out methods of the Hamamatsu array using the BC-408 plastic scintillator, a ^{133}Ba source (gammas with 81 - 356 keV) and the same bias voltage of 57.6 V for all measurements. The amount of simultaneously read out channels increases the SNR (Pulse height/FWHM).

3.2.6. Spectra measured with the Hamamatsu Array

To investigate the effect of different readout methods of the Hamamatsu array on a spectrum, two measurements were performed at room temperature using distinct readout techniques. For these measurements, the BC-408 plastic scintillator has been used together with the ^{137}Cs source (662 keV gammas). The bias current was set to 7.2 µA since this showed the best SNR. The measuring time was set to 1 h. The MCA was set to the range of 1 V for the 8192 Channels. Figure 3.23 shows the spectrum recorded with one individual SiPM (A1). The counts of the individual channels have been normalized to the total number of counts.

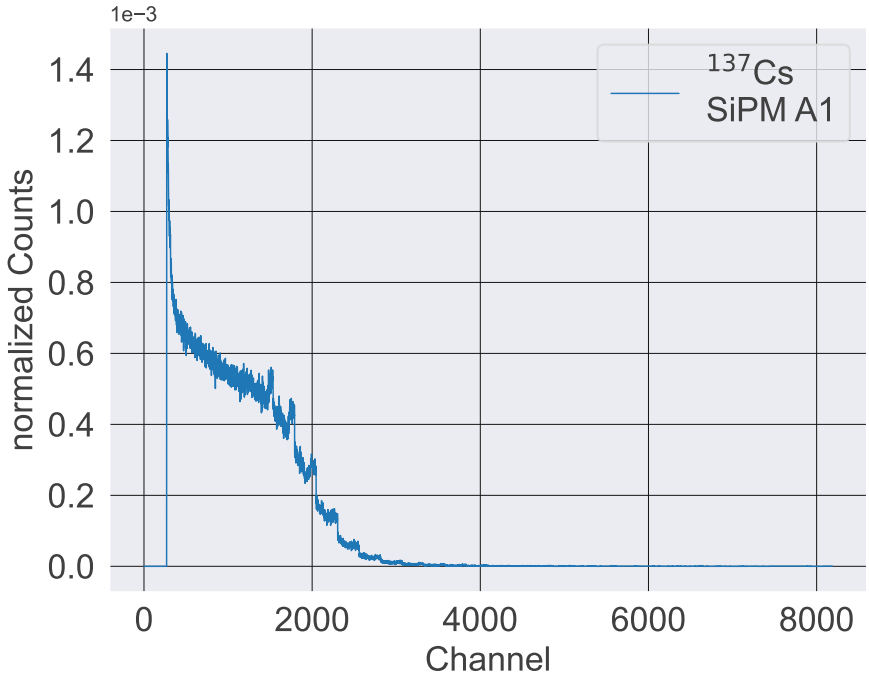

Figure 3.23.: Spectrum of the ^{137}Cs source (662 keV gammas) recorded the SiPM A1 of the Hamamatsu array read out individually at 7.2 µA bias current using the BC-408 plastic scintillator. The counts have been normalized to the total number of counts. Measurement time: 1 h. Number of channels: 8192

By fitting a Gaussian function (see Eq. 3.2) to the Compton edge of ^{137}Cs (at about 447 keV) the position of the peak was found to be at channel 1354. This feature has been selected for the comparison of the readout methods. Figure 3.24 shows the spectrum recorded with the whole 16-SiPM unit read out simultaneously. This shifted the peak position at the Compton edge by a factor of 4 to channel 5777. This is consistent with the factor of 4, which increased pulse height from

individual readout to the readout of the 16-SiPM unit. The photoelectric peak at 662 keV is not present in the ^{137}Cs spectrum since this energy is too high to be fully absorbed by the BC-408 plastic scintillator.

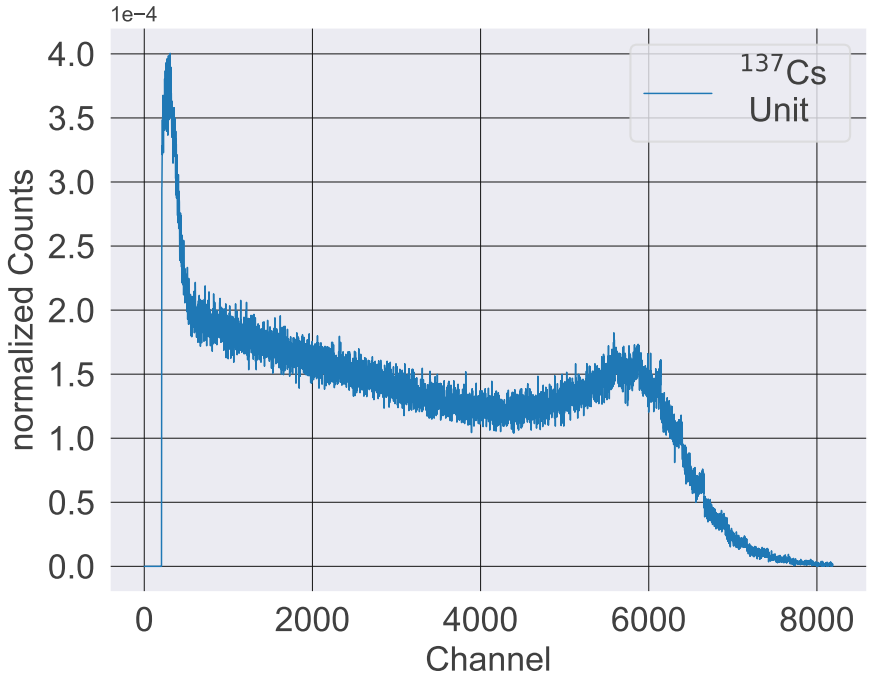

Figure 3.24.: Spectrum of the ^{137}Cs source (662 keV gammas) recorded with all 16 SiPMs of the Hamamatsu array read out simultaneously at 7.2 µA bias current using the BC-408 plastic scintillator. The counts have been normalized to the total number of counts.Measurement time: 1 h. Number of channels: 8192

The extracted data from the fits of these two measurements is given in table 3.9. In addition to the measurements with BC-408 and ^{137}Cs, a spectrum of ^{133}Ba has been recorded with the YSO crystal. YSO was shown to be the brightest crystal with the best SNR (see Section 3.2.3). The measurement of ^{133}Ba (gammas with 81 - 356 keV) was performed over a period of 6 h with the SiPM A1 of the Hamamatsu array read out individually. The two peaks of the ^{133}Ba spectrum are located at channels 265 and 762. Since for this measurement, only 4096 channels were used, one has to multiply these numbers by a factor of 2 to have an estimate of the position relative to the other measurements. This leads to estimated peak positions at channels 530 and 1524.

^{137}Cs	Peak Position [Ch.]	FWHM [Ch.]
1 SiPM	1354	1253
16 SiPMs	5777	1427

Table 3.9.: Data extracted from fits of the spectra of the ^{137}Cs source (662 keV gammas) recorded with one individual SiPM (A1) and all 16 SiPMs of the Hamamatsu array read out simultaneously at 7.2 µA bias current using the BC-408 plastic scintillator. Measurement time: 1 h. Number of channels: 8192

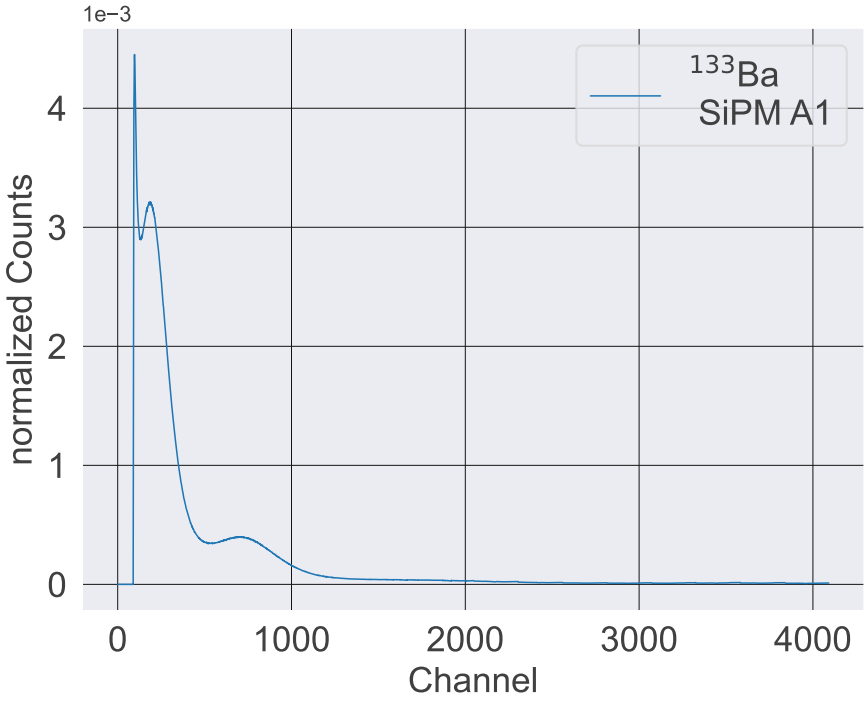

Figure 3.25.: Spectrum of the ^{133}Ba source (gammas with 81 - 356 keV) recorded the SiPM A1 of the Hamamatsu array read out individually at 7.2 µA bias current using the YSO crystal. The counts have been normalized to the total number of counts. Measurement time: 6 h. Number of channels: 4096

3.3. Measurements with the AdvanSiD SiPM(NUV)

The NUV SiPM ($3\times3\,\mathrm{mm}^2$) from AdvanSiD [31] has been used for the development of the cooling system.

Gain Dependency on Temperature and Bias Current

Since the breakthrough voltage of the detection system is temperature dependent, and the gain of the system is proportional to the overvoltage applied, one has to establish a stable temperature during a measurement. At the same time, the bias current of the 4-channel amplifying board can be used to control the supplied voltage and, therefore, the gain. However, gain itself is temperature-dependent, which reinforces the importance of thermally stable conditions.

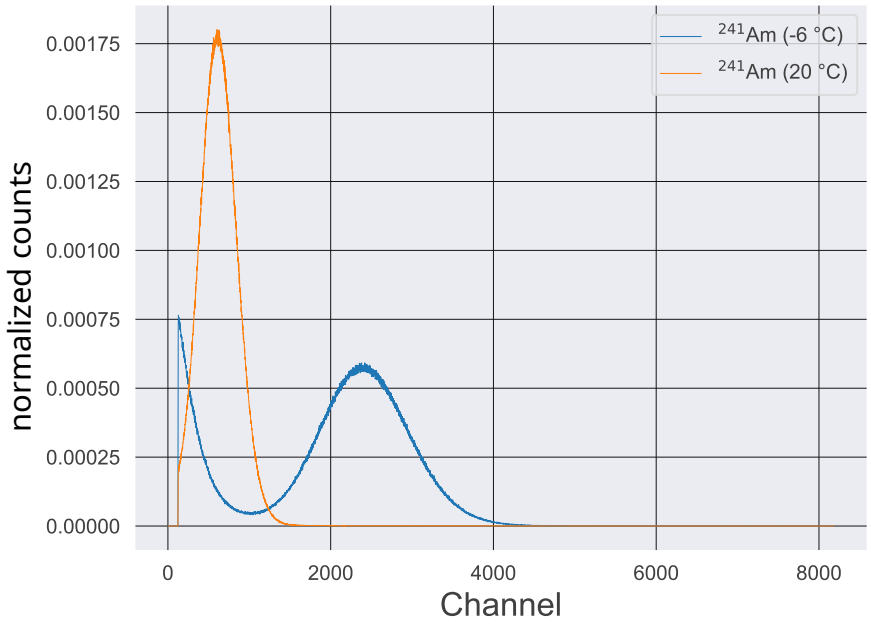

Figure 3.26.: Effective change in gain of the detection system with a temperature change of $\Delta T = 26\,^{\circ}\mathrm{C}$. The orange line represents the spectrum at room temperature while the blue line is measured at $-6\,^{\circ}\mathrm{C}$. The Spectra are recorded with the NUV SiPM, the YSO-crystal, the ^{241}Am source (60 keV gammas) and 5.2 µA. Counts were normalized to the total amount of counts.

To demonstrate and characterize the individual effects of the bias current and the temperature, two series of measurements were performed: 1) at a stable temperature with a changing bias current and 2) with a fixed bias current but at different temperatures. Figure 3.26 shows the spectra of the ^{241}Am source described in table 2.4. Both spectra have been recorded over 6 h. The temperature fluctuations ($\delta T = 2\,^{\circ}\mathrm{C}$) of both measurements lie within the fluctuations of the ambience during the measuring time and can be neglected. The orange spectrum has been recorded without the coldfinger being connected to a heat sink and therefore at room temperature (20 °C). The spectrum depicted in blue, on the other hand, has been recorded at −6 °C. The bias current has been set to 5.2 µA for both measurements. Cooling down the detector by 20 °C shifted the main emission peak approximately from channel 600 to channel 2400 and, therefore, by a factor of 4, while the peak height was reduced by a factor of 3. Since this is more of a qualitative demonstration of this behaviour, no fit has been performed to obtain numerical values. But this leaves room for further investigations with the Hamamatsu MPPC array in future work.
The spectra recorded with different bias currents (2.8 µA, 5.2 µA and 7.0 µA) can be seen in Figure 3.27. It displays the increasing gain of the system with increasing bias current.
The source used for these measurements was the ^{133}Ba source (gammas with 81 - 356 keV) and the measuring time was 6 h. Each spectrum consists of two peaks. The first peak of each spectrum comes from gammas with 81 keV and the second peak from emitted gammas above 300 keV. By comparing, for example, the second peak of each spectrum, it can be observed that the peak position shifts from channel 2000 (2.8 µA), to channel 3700 (5.2 µA) and for the highest bias current to channel 5000 (7.2 µA). This is caused by the higher gain of the SiPM with a higher overvoltage. At the same time, the FWHM of the same peaks increases from about 400 channels (2.8 µA) up to 1500 channels. Since with 2.8 µA the 81 keV peak is already close to the background, and the ^{241}Am source used for the temperature measurements emits gammas at 60 keV, the default value for the NUV SiPM has been set to 5.2 µA to be able to record spectra with ^{241}Am.

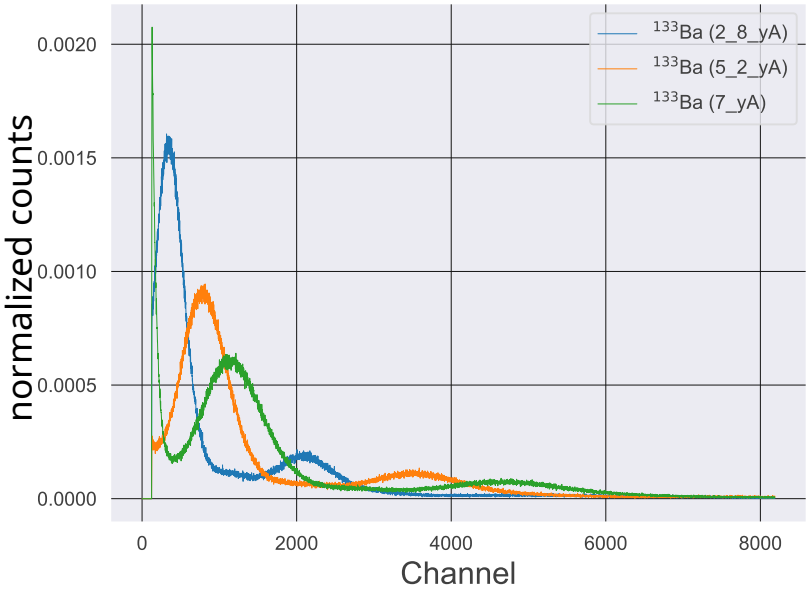

Figure 3.27.: Three measurements performed with the NUV SiPM, the YSO crystal, a ^{133}Ba source (gammas with 81 - 356 keV) and with increasing bias current. The peaks of the spectra show a shift towards the higher channels when increasing the current. The green line shows a spectrum recorded with 7 µA, the orange line shows a spectrum recorded with 5.2 µA, and the blue spectrum has been recorded with 2.8 µA. The spectra were recorded at room temperature (21 °C).

3.3.1. Pulse Shape

As could be seen in all measurements from section 3.2, the collected pulses show an undershoot on the falling side. This behaviour is produced by the electronics on purpose since this was part of their original function. Figure 3.28 shows the same behaviour occurring with the 4-channel amplifying board and the NUV SiPM. This is an indicator that the undershoot is produced by the electronics and not by the Hamamatsu MPPC array. This undershoot increases the signal duration (from the rise of the pulse until the end of the undershoot) to almost 5 µs, while the signal width of the pulse itself is about 0.5 µs.

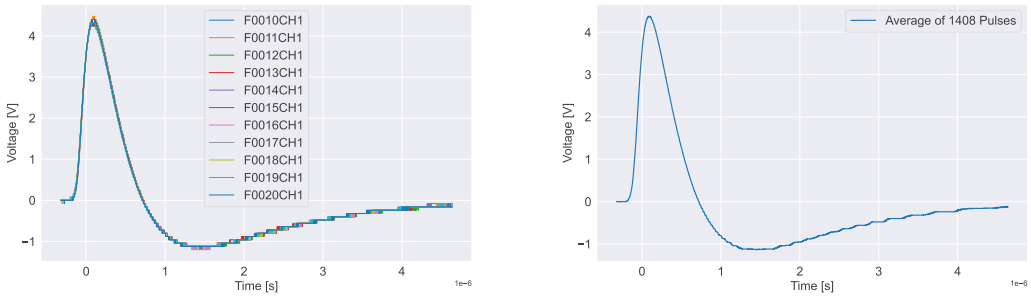

Figure 3.28.: Pulses recorded from an ^{241}Am source (gammas with 60 keV) with the NUV SiPM, at room temperature, the YSO scintillator and with 5.2 µA. The left plot displays the individual measurements, each containing an average of 128 pulses. The right plot is the average of all measurements.

3.3.2. Temperature Stability

To test if the cooling system provides stable conditions at −6 °C for six hours, a series of six measurements - each of them over the timespan of one hour - has been performed. All measured spectra are shown in Figure 3.27, the pink line is the average of the other spectra combined. Since this was a rough estimate to identify possible problems with the cooling, which would cause a drift in the spectrum, no fit was calculated with this data. In the observed six hours, the position of the main emission peak (60 keV gammas) of the 1 h measurements has fluctuated by about 100 channels from the position of the peak of the 6 h long measurement. This gives an average peak position of about 2400 ± 100 channels which is acceptable for the temperature fluctuations being of the order of 2 °C.

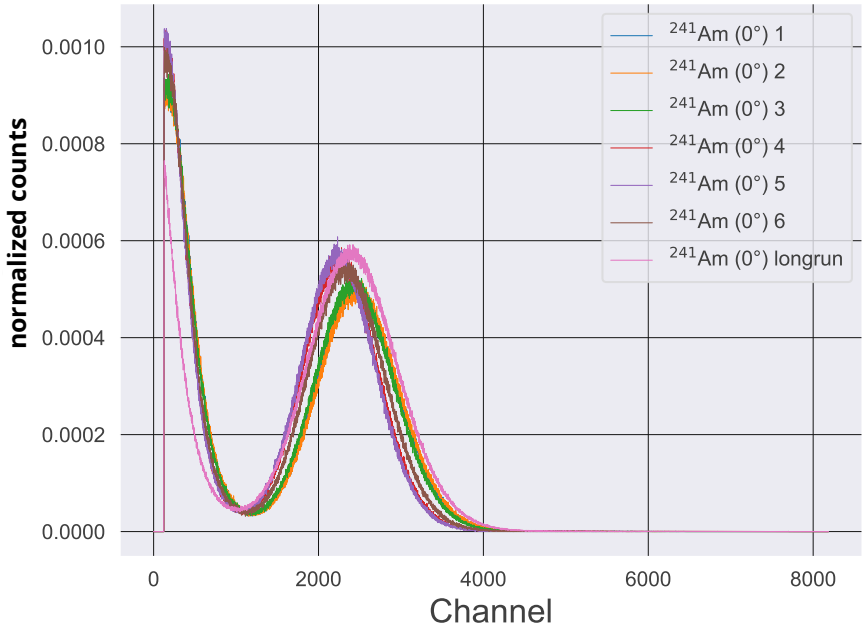

Figure 3.29.: Spectra of ^{241}Am recorded with 5.2 µA bias current at −6 °C. The NUV SiPM with the YSO crystal has been used for these measurements. The different measurements cover a time of six hours, each line representing a spectrum recorded for one hour.

4. Conclusions and Outlook

Within the scope of this thesis, an experimental setup has been built that allows testing the capabilities of SiPMs and SiPM arrays. Part of this setup is the in-house developed adapter PCB that allows to access all 16 SiPMs of one Hamamatsu unit individually. This adapter is shown in Figure 2.2 together with the 16-channel amplifying board provided by the SMI [53] and the BC-408 plastic scintillator used for various measurements. The stripboard in the middle was used for the collective measurements of the Hamamatsu MPPC array. The amplifying board provided stable conditions throughout the measurements and is an option for PERC to compare the stability of readout electronics.

Various measurements documented the influence of the scintillator material (BC-408, BGO, YSO), the bias Voltage V_{bias}, cables, read-out patterns, and temperature on the output signal of a SiPM. To find the parameters suitable for the measurements, a series of measurements with the same individual SiPM (A1), scintillator (BGO), and source (^{137}Cs) at different bias currents has been performed. The bias current was increased in steps of 0.4 µA. From 6.4 µA to 8.0 µA, this increase in bias current leads to an increase in the pulse height by a factor of 3. For the measurement with 7.6 µA, the pulse height increased by a factor of 1.2 compared to the measurement with 7.2 µA. Due to this behaviour, the SNR was better by a factor of 2 for 7.2 µA, which is why this value of the bias current was chosen for all other measurements.

Due to the rise time in the order of ns and the similarity to the scintillator that is going to be used for the main detector of PERC (BC-404), BC-408 has been chosen for a majority of the measurements. The gain of SiPM A1 of the Hamamatsu array - measured with 7.2 µA, the ^{133}Ba source (gammas with 81 - 356 keV) and BC-408 - fluctuated by 3.9% of the pulse height over a two-day period. This corresponds to a standard deviation of 5.2 mV for the pulse height. This deviation is acceptable given the ambient temperature fluctuations of $\Delta T = 2\,^{\circ}\mathrm{C}$ and the temperature coefficient of the breakdown voltage of $\Delta T(V_{op}) = 54\,\mathrm{mV}\,^{\circ}\mathrm{C}^{-1}$ for the Hamamatsu array.

With the same setup (SiPM A1, 7.2 µA, ^{133}Ba source and BC-408), 8 out of the 16 SiPMs of the array have been measured individually. The average rise time of the resulting pulse is $\tau_r = 9.27 \pm 0.49$ ns and the pulse height is 226.7 ± 20.0 mV. The

calculated standard deviation of the averaged pulses of the individual SiPMs is equivalent to ±8.8 % of the pulse height. The measured rise time of the individual measurements with BC-408 has a σ of ±5.1 %. This non-uniformity shows that if one wants to read out the SiPMs individually, each SiPM has to be characterized.

With the same bias current, BGO produced an averaged pulse with a rise time of $\tau_r = 41.68\,\text{ns}$ and YSO produced an averaged pulse with a rise time of $\tau_r = 34.83\,\text{ns}$. As expected from the known properties of these scintillators, BC-408 has the fastest rise time. At the same time, the averaged pulse of YSO had a pulse height that was a by a factor of 5 higher (1084 mV) compared to the other scintillators. This means that the light yield of the YSO crystal is 5 times higher. If it is produced in large enough dimensions, YSO is an alternative material that could be used for the PERC detector instead of BC-404.

By connecting groups of 4 SiPMs and reading them out simultaneously, the average rise time grew by a factor of 2 ($\tau_r = 18.36\,\text{ns}$) using BC-408, the ^{133}Ba source and the same bias voltage (57.6 V) as for the individual measurements. The average peak height increased from 111.1 mV to 252.0 mV by a factor of 2.3 compared to the individual readout. When the whole 16-SiPM unit is read out simultaneously, the rise time is increased by another factor of 2, reaching 39.04 ns. The pulse height also increased to an average of 317.4 mV. Since the ToF for backscattering events at PERC is of the order of 50 ns, these averaged rise times are still acceptable. But the measurements with the 16 channels simultaneously read out included one averaged pulse with a rise time above 50 ns, which leaves room for further measurements to increase the statistics for the average rise time of the whole unit.

Another important aspect of the readout of a SiPM array is the SNR of the system. For this purpose, the noise level of the pre-trigger region has been analyzed in different scenarios (cable length, bias current, readout method). The twisted pairs of cables used to connect the SiPMs to the power supply and the power supply to the ADC have been checked up to a length of 1.9 m. There has been observed no significant change in their noise level from 0.75 m to 1.9 m. For SiPM A1 with a bias current of 7.2 µA, the BC-408 scintillator and a ^{137}Cs source (662 keV gammas), the average peak height is 226.7 mV. For this setup, the 0.75 cm cable had a noise level in the pre-trigger region of 3.38 mV and the 1.9 m cable had a noise level of 3.05 mV. The difference relative to the peak height is about 0.2% and, therefore, negligible.

The collective readout methods showed an increase in their SNR with the number of connected SiPMs. The average SNR for the individual readout was 42.9. This

increased for the collective readout of 4 SiPMs by a factor of 1.4 to an average SNR of 58.2, and for the simultaneous readout of the whole unit, the SNR increased by almost a factor of 2 to 76.1 compared to the individual readout. The effect of the prolonged pulse duration was visible in the spectra recorded with the different readout methods of the Hamamatsu array. By comparing the spectrum recorded with one individual SiPM (A1) with the spectrum recorded with the whole 16-SiPM unit read out simultaneously, the position of the Compton edge of ^{137}Cs ($\approx$ 447 keV) changed by a factor of 4 towards the higher channels of the MCA. This is consistent with the increase of the pulse height by a factor of 4.

As shown in the measurements performed with the NUV SiPM, a stable temperature is important for using a SiPM in spectroscopy. Additionally, cooling down the system improves the noise level due to the lower dark count rate and brings an effective increase in the gain of the system. Similar measurements at a low temperature ($\mathcal{O}(-5°C)$) can provide information on how strong these effects are on the Hamamatsu SiPM array. Furthermore, since the array has a larger surface and consists of 16 individual SiPMs, it is necessary to see if it is possible to reach an equilibrium temperature for the whole array or to have a measure of how much the temperature fluctuates across the array. Another interesting aspect would be to analyze the differences between two different Hamamatsu MPPC arrays. Since the read-out method (individual or collective) chosen for the SiPMs had an influence on the recorded pulse shape, it would be of interest to see how much the results from the two independent arrays differ. The prototype of one PERC backscatter detector (shown in Figure 4.1), is planned to consist of an array of 20 Hamamatsu SiPM arrays.

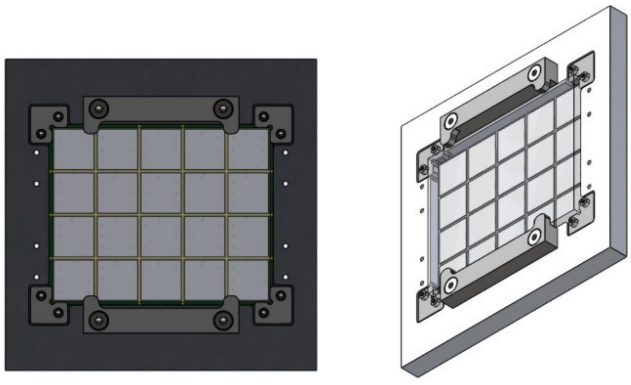

Figure 4.1.: Schematic of the prototype of the secondary detector, showing an array of 4 $\times$ 5 Hamamatsu SiPM units. Taken from [15].

The prototype consists of 320 individual SiPMs, which will be read out in groups of 4 SiPMs. This reduces the amount of cables necessary for the readout and, therefore, the possible pick-up noise. These 80 groups need to be synchronized in terms of their gain if one wants to prevent a smear-out in the energy spectrum. For the final backscatter detector system, consisting of 3200 SiPMs, one would need to perform an energy calibration for each SiPM to increase the SNR of the final backscattered electron spectrum, if one wants to read them out individually.

Bibliography

[1] G. Aad et al., "Observation of a new particle in the search for the standard model higgs boson with the atlas detector at the lhc", Physics Letters B **716**, 1–29 (2012) (cited on page 1).

[2] P. W. Higgs, "Broken symmetries and the masses of gauge bosons", Phys. Rev. Lett. **13**, 508–509 (1964) (cited on page 1).

[3] M. Gorchtein and C.-Y. Seng, "The standard model theory of neutron beta decay", Universe **9**, 422 (2023) (cited on page 1).

[4] B. Fornal and B. Grinstein, "Dark matter interpretation of the neutron decay anomaly", Phys. Rev. Lett. **120**, 191801 (2018) (cited on page 1).

[5] D. Dubbers, H. Saul, B. Märkisch, T. Soldner, and H. Abele, "Exotic decay channels are not the cause of the neutron lifetime anomaly", Physics Letters B **791**, 10.1016/j.physletb.2019.02.013 (2019) (cited on page 2).

[6] M. Kobayashi and T. Maskawa, "CP-Violation in the Renormalizable Theory of Weak Interaction", Progress of Theoretical Physics **49**, 652–657 (1973) (cited on page 1).

[7] N. Cabibbo, "Unitary symmetry and leptonic decays", Phys. Rev. Lett. **10**, 531–533 (1963) (cited on page 1).

[8] K. Bernert, J. Klenke, M. Lebert, K. Lehmann, and B. Märkisch, *The spectrometer PERC and its backscatter detector system*, Ecole Joliot Curie: "Beyond the Standard Model of Weak Interaction : nuclei, neutrons and neutrinos", Saint-Pierre d'Oléron (France), 2023 (cited on pages 1, 5).

[9] B. Märkisch, H. Abele, D. Dubbers, F. Friedl, A. Kaplan, H. Mest, M. Schumann, T. Soldner, and D. Wilkin, "The new neutron decay spectrometer perkeo iii", Nuclear Instruments and Methods in Physics Research Section A: Accelerators, Spectrometers, Detectors and Associated Equipment **611**, Particle Physics with Slow Neutrons, 216–218 (2009) (cited on page 2).

[10] B. Märkisch et al., "Measurement of the weak axial-vector coupling constant in the decay of free neutrons using a pulsed cold neutron beam", Phys. Rev. Lett. **122**, 242501 (2019) (cited on page 2).

[11] B. Märkisch, H. Saul, D. Dubbers, H. Abele, and T. Soldner, "Accurate measurement of the beta asymmetry in neutron decay rules out dark decay mode", in , Vol. 14 (Oct. 2020) (cited on pages 2, 4).

[12] D. Dubbers and B. Märkisch, "Precise measurements of the decay of free neutrons", Annual Review of Nuclear and Particle Science **71**, 139–163 (2021) (cited on page 3).

[13] D. Dubbers, H. Abele, S. Baeßler, B. Märkisch, M. Schumann, T. Soldner, and O. Zimmer, "A clean, bright, and versatile source of neutron decay products", Nuclear Instruments and Methods in Physics Research Section A: Accelerators, Spectrometers, Detectors and Associated Equipment **596**, 238–247 (2008) (cited on page 2).

[14] X. Wang et al., "Design of the magnet system of the neutron decay facility PERC", EPJ Web Conf. **219**, 04007 (2019) (cited on page 2).

[15] K. Bernert, J. Klenke, M. Lebert, K. Lehmann, and B. Märkisch, *A prototype for the backscatter detector system of PERC*, MLZ User Meeting 2023, Munich (Germany), 2023 (cited on pages 3–5, 19, 63).

[16] K. Bernert, "Electron spectroscopy in neutron beta decay", To be published, PhD thesis (Technical University of Munich, Garching, Germany, Example City, CA, 2024) (cited on page 4).

[17] E. Fermi, "Versuch einer Theorie der β-Strahlen. I", Zeitschrift für Physik **88**, 161–177 (1934) (cited on page 6).

[18] P. D. Group et al., "Review of particle physics", Progress of Theoretical and Experimental Physics **2022**, 083C01 (2022) (cited on page 6).

[19] M. Lamparth, "Fierz interference term in neutron beta decay and new approaches for systematic uncertainty quantification", en, PhD thesis (Technische Universität München, 2023), page 147 (cited on page 6).

[20] D. H. Wilkinson, "Analysis of Neutron Beta Decay", Nucl. Phys. A **377**, 474–504 (1982) (cited on page 7).

[21] J. D. Jackson, S. B. Treiman, and H. W. Wyld, "Possible tests of time reversal invariance in beta decay", Phys. Rev. **106**, 517–521 (1957) (cited on page 7).

[22] H. Saul, C. Roick, H. Abele, H. Mest, M. Klopf, A. K. Petukhov, T. Soldner, X. Wang, D. Werder, and B. Märkisch, "Limit on the fierz interference term b from a measurement of the beta asymmetry in neutron decay", Phys. Rev. Lett. **125**, 112501 (2020) (cited on page 7).

[23] G Konrad et al., "Neutron decay with perc: a progress report", Journal of Physics: Conference Series **340**, 012048 (2012) (cited on page 8).

[24] C.-Y. Seng, "Testing effective field theory with the most general neutron decay correlations", Physical Review D **109**, 10.1103/PhysRevD.109.073007 (2024) (cited on page 8).

[25] P. Tandon, D. Prakash, S. C. Kheruka, and N. N. Bhat, "Interaction of ionizing radiation with matter", in *Radiation safety guide for nuclear medicine professionals* (Springer Nature Singapore, Singapore, 2022), pages 21–35 (cited on page 8).

[26] N. Bohr, "Ii. on the theory of the decrease of velocity of moving electrified particles on passing through matter", The London, Edinburgh, and Dublin Philosophical Magazine and Journal of Science **25**, 10–31 (1913) (cited on page 8).

[27] M. Berger, J. Coursey, M. Zucker, and J. Chang, *Estar, pstar, and astar: computer programs for calculating stopping-power and range tables for electrons, protons, and helium ions (version 1.2.3).* http://physics.nist.gov/Star, [Accessed 01-May-2024], 2005 (cited on page 8).

[28] "Stopping powers for electrons and positrons. [26 elements, 49 compounds and mixtures]", (1984) (cited on pages 9–10).

[29] A. Garcia and E. Henley, *Subatomic physics (3rd edition)* (World Scientific Publishing Company, 2007) (cited on page 10).

[30] F. Acerbi and S. Gundacker, "Understanding and simulating sipms", Nuclear Instruments and Methods in Physics Research Section A: Accelerators, Spectrometers, Detectors and Associated Equipment **926**, Silicon Photomultipliers: Technology, Characterisation and Applications, 16–35 (2019) (cited on pages 12–13).

[31] P. Buzhan et al., "The advanced study of silicon photomultiplier", 10.1142/9789812776464_0101 (2002) (cited on pages 12, 56).

[32] D. J. Herbert, V. Saveliev, N. Belcari, N. D'Ascenzo, A. Del Guerra, and A. Golovin, "First results of scintillator readout with silicon photomultiplier", IEEE Transactions on Nuclear Science **53**, Cited by: 78, 389 – 394 (2006) (cited on page 12).

[33] P. Hariharan, "Chapter 7 - detectors", in *Basics of interferometry*, edited by P. Hariharan (Academic Press, San Diego, 1992), pages 57–65 (cited on page 12).

[34] I. Abt, "Silicon detectors", in *Techniques and concepts of high energy physics x*, edited by T. Ferbel (Springer Netherlands, Dordrecht, 1999), pages 295–333 (cited on page 12).

[35] J. J. McKendry, E. Gu, N. McAlinden, N. Laurand, K. Mathieson, and M. D. Dawson, "Chapter two - micro-leds for biomedical applications", in *Micro leds*, Vol. 106, edited by H. Jiang and J. Lin, Semiconductors and Semimetals (Elsevier, 2021), pages 57–94 (cited on page 13).

[36] M.-J. Lee, "Single-photon avalanche diodes in cmos technology: towards low-cost and compact solid-state lidar sensors", in Optical sensors and sensing congress (2020), ETu3E.2 (cited on page 13).

[37] M. Ghioni, G. Armellini, P. Maccagnani, I. Rech, M. Emsley, and M. S. ünlü, "Resonant-cavity-enhanced single-photon avalanche diodes on reflecting silicon substrates", Photonics Technology Letters, IEEE **20**, 413 –415 (2008) (cited on page 13).

[38] S. Cova, M. Ghioni, A. Lacaita, C. Samori, and F. Zappa, "Avalanche photodiodes and quenching circuits for single-photon detection", Appl. Opt. **35**, 1956–1976 (1996) (cited on page 13).

[39] C. Piemonte, F. Acerbi, A. Ferri, A. Gola, G. Paternoster, V. Regazzoni, G. Zappala, and N. Zorzi, "Performance of nuv-hd silicon photomultiplier technology", IEEE Transactions on Electron Devices **63**, 1111–1116 (2016) (cited on page 13).

[40] AdvanSiD, *AdvanSiD: Advanced Silicon Detectors — advansid.com*, `https://www.advansid.com/`, [Accessed 06-Jun-2023], 2023 (cited on page 13).

[41] Advansid, *Nuv - silicon photomultiplier datasheet*, `https://www.advansid.com/`, 2016 (cited on pages 13–15).

[42] H. Photonics, `https://www.hamamatsu.com`, [Accessed 20-Dec-2023], 2023 (cited on page 15).

[43] H. Photonics, `https://www.hamamatsu.com/content/dam/hamamatsu-photonics/sites/documents/99_SALES_LIBRARY/ssd/s13361-3050_series_kapd1054e.pdf`, [Accessed 04-Jan-2024], 2023 (cited on pages 15–16, 30, 34, 40, 42).

[44] J. B. Birks, *The theory and practice of scintillation counting: international series of monographs in electronics and instrumentation*, Vol. 27 (Elsevier, 2013) (cited on pages 18, 28).

[45] J. B. Birks, "Scintillations from organic crystals: specific fluorescence and relative response to different radiations", Proceedings of the Physical Society. Section A **64**, 874 (1951) (cited on page 18).

[46] Epic-crystal, `https://www.epic-crystal.com/data/upload/20181120/5bf3cfb5463aa.pdf`, [Accessed 06-Jun-2023] (cited on pages 18–19, 35).

[47] M. Globus, B. Grinyov, and J. Kim, *Inorganic scintillators for modern and traditional applications* (Institute for Single Crystals, 2005) (cited on pages 18–19, 35).

[48] E. Sakai, "Recent measurements on scintillator-photodetector systems", IEEE Transactions on Nuclear Science **34**, 418–422 (1987) (cited on pages 18–19, 35).

[49] H Ishibashi, K Kurashige, Y Kurata, K Susa, M Kobayashi, M Tanaka, K Hara, and M Ishii, "Scintillation performance of large ce-doped gdsub 2siosub 5 (gso) single crystal", IEEE Transactions on Nuclear Science **45**, 10.1109/23.682439 (1998) (cited on pages 18, 35).

[50] K. Popovich, M. Šípková, V. Čuba, L. Procházková, J. Bárta, and M. Nikl, "Highly luminescent cerium-doped yso/ lso microcrystals prepared via room temperature sol-gel route", Radiation Measurements **122**, 84–90 (2019) (cited on page 19).

[51] R. Components, *Datasheet: product information*, Accessed: 2024-05-16, 2024 (cited on page 19).

[52] Amptek, *Mca-8000d digital multichannel analyzer – amptek – x-ray detectors and electronics*, https://www.amptek.com/products/multichannel-analyzers/mca-8000d-digital-multichannel-analyzer, [Accessed 13-Jun-2023] (cited on page 20).

[53] Stefan Meyer Institute of Subatomic Physics and Marlene Tüchler and Johann Zmeskal, *Equipment Loan*, Equipment loaned for research purposes. Personal communication., 2024 (cited on pages 20–22, 61).

[54] G. E. GmbH, *Digital multi channel analyzer mca527*, https://www.gbs-elektronik.de/media/download_gallery/MCA527_Flyer.pdf, [Accessed 02-May-2024] (cited on page 20).

[55] M. Tüchler, "Probing the strong interaction with kaonic atom X-ray measurements at low energies", PhD thesis (Vienna U., 2023) (cited on page 21).

[56] M. Tüchler, "A charged particle veto detection system for kaonic deuterium measurements at daφne", en, 10.25365/THESIS.56347 (2019) (cited on page 21).

[57] Tektronix, https://download.tek.com/datasheet/TDS2000C-Digital-Storage-Oscilloscope-Datasheet-3GW256458.pdf, [Accessed 01-May-2024], 2019 (cited on page 21).

[58] M.-M. Bé et al., *Table of radionuclides*, Vol. 5, Monographie BIPM-5 (Bureau International des Poids et Mesures, Pavillon de Breteuil, F-92310 Sèvres, France, 2010) (cited on page 25).

[59] M.-M. Bé, V. Chisté, C. Dulieu, X. Mougeot, V. Chechev, F. Kondev, A. Nichols, X. Huang, and B. Wang, *Table of radionuclides*, Vol. 7, Monographie BIPM-5 (Bureau International des Poids et Mesures, Pavillon de Breteuil, F-92310 Sèvres, France, 2013) (cited on page 25).

[60] M.-M. Bé et al., *Table of radionuclides*, Vol. 8, Monographie BIPM-5 (Bureau International des Poids et Mesures, Pavillon de Breteuil, F-92310 Sèvres, France, 2016) (cited on page 25).

[61] R. Van Ammel, S. Pommé, J. Paepen, and G. Sibbens, "Measurement of the 109cd half-life", Applied Radiation and Isotopes **69**, 785–789 (2011) (cited on page 25).

[62] T. pandas development team, "Pandas-dev/pandas: pandas", `10.5281/zenodo.7857418` (2023) (cited on page 27).

[63] P. Virtanen et al., "SciPy 1.0: Fundamental Algorithms for Scientific Computing in Python", Nature Methods **17**, 261–272 (2020) (cited on page 27).

[64] Saint-Gobain, *Plastic scintillators bc-400, bc-404, bc-408, bc-412, bc-416 data sheet*, Accessed: 2024-05-26, 2017 (cited on page 40).

A. Averaged Pulses

A.1. Bias Current Data

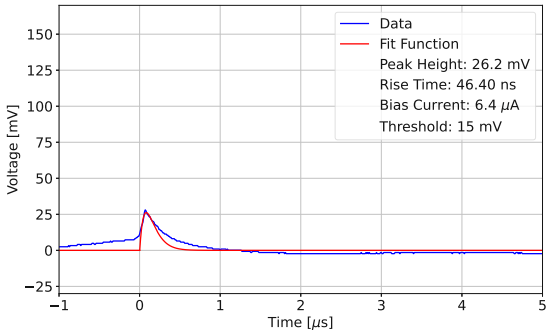

Figure A.1.: SiPM pos.: A1,
Source: ^{137}Cs,
Scintillator: BGO,
I_{Bias} =6.4 µA

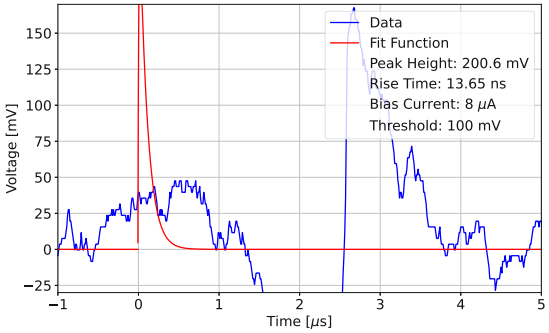

Figure A.2.: SiPM pos.: A1,
Source: ^{137}Cs,
Scintillator: BGO,
I_{Bias} =8.0 µA

A.2. BGO, 7.2 µA, Source: ^{137}Cs

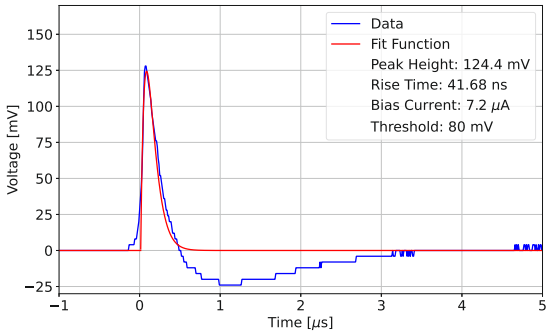

Figure A.3.: SiPM pos.: A1

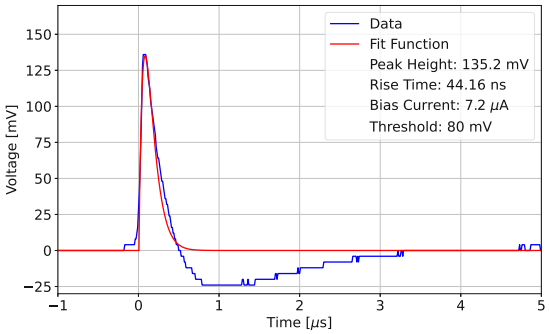

Figure A.4.: SiPM pos.: A2

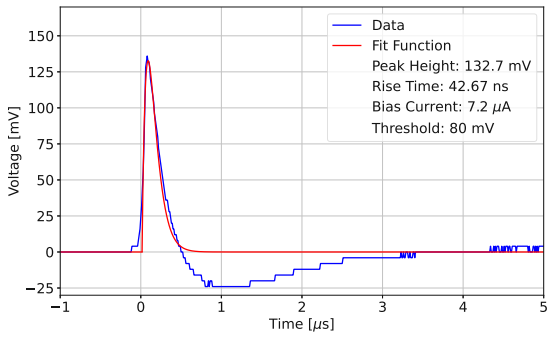

Figure A.5.: SiPM pos.: A3

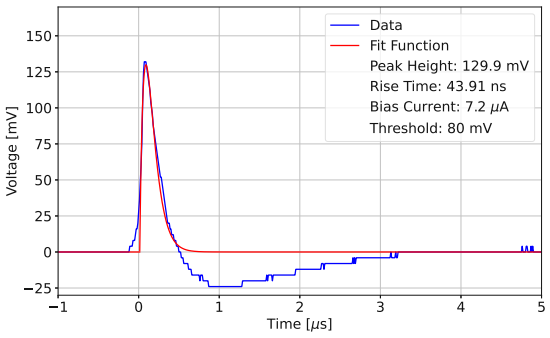

Figure A.6.: SiPM pos.: A4

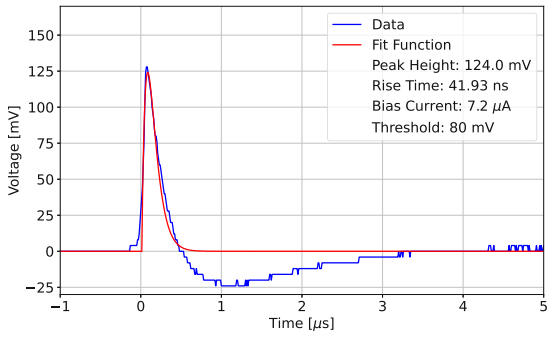

Figure A.7.: SiPM pos.: B1

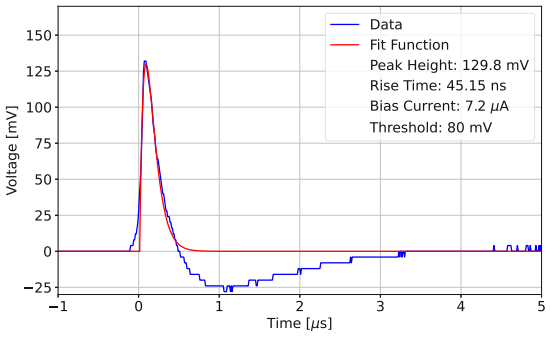

Figure A.8.: SiPM pos.: B2

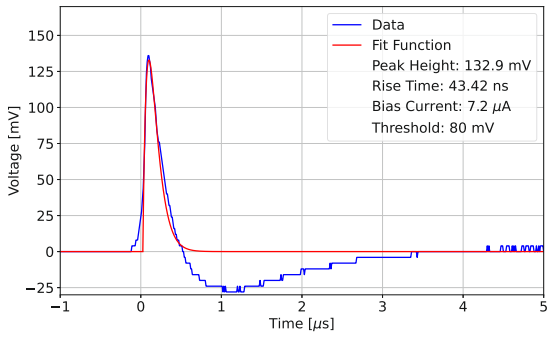

Figure A.9.: SiPM pos.: B3

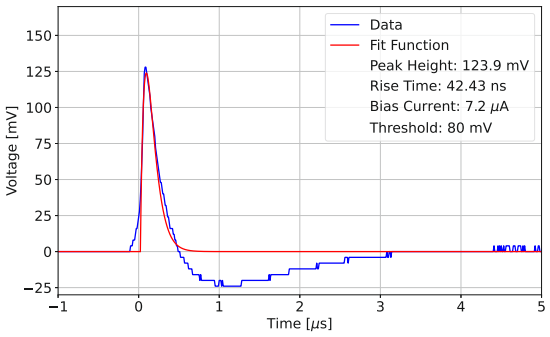

Figure A.10.: SiPM pos.: B4

A.3. BC-408, 7.2 µA, Source: ^{137}Cs

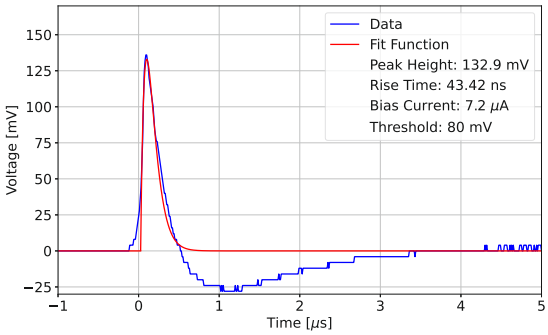

Figure A.11.: SiPM pos.: A1

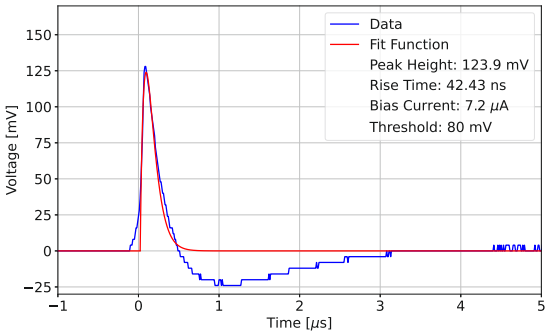

Figure A.12.: SiPM pos.: A3

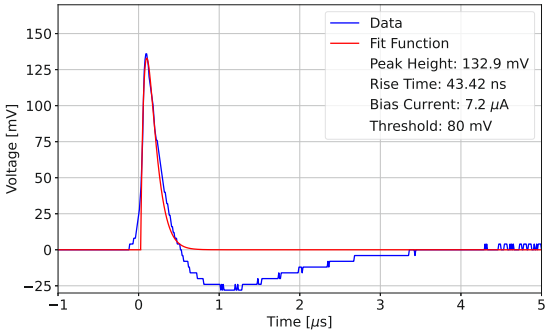

Figure A.13.: SiPM pos.: B2

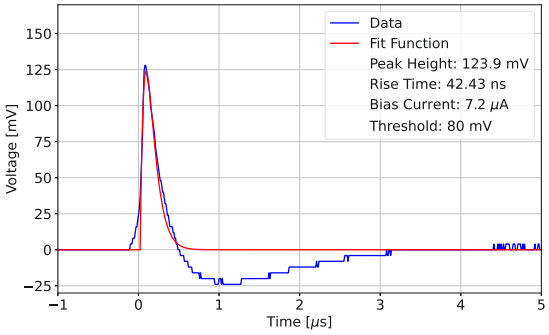

Figure A.14.: SiPM pos.: B4

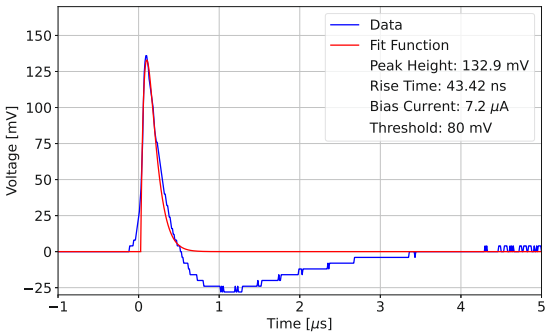

Figure A.15.: SiPM pos.: C1

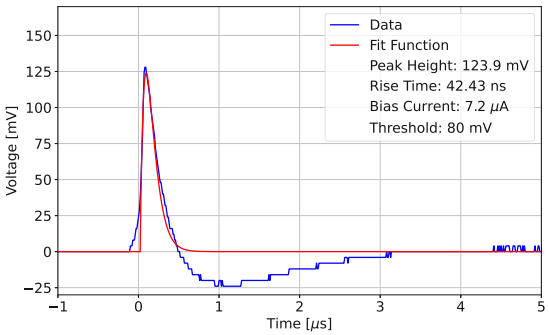

Figure A.16.: SiPM pos.: C3

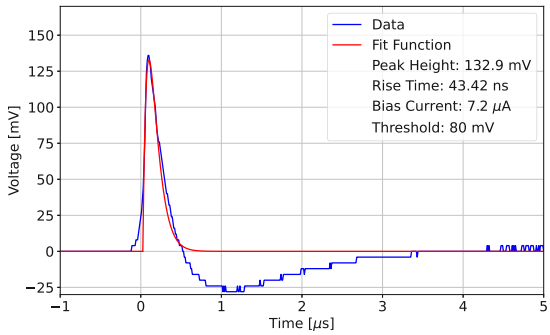

Figure A.17.: SiPM pos.: D2

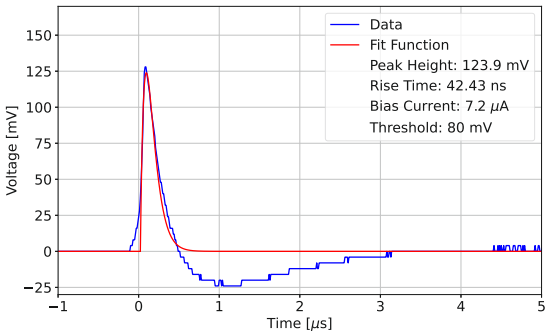

Figure A.18.: SiPM pos.: D4

A.4. Groups of four SiPMs, Source: ^{133}Ba

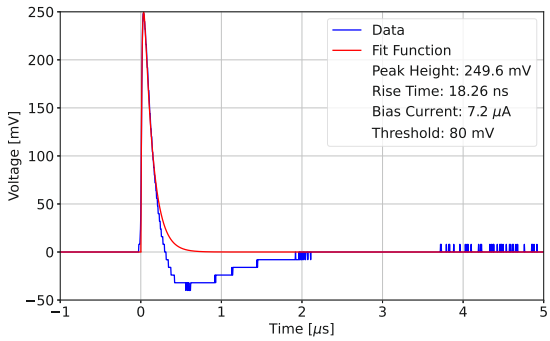

Figure A.19.: SiPM pos.: AB12

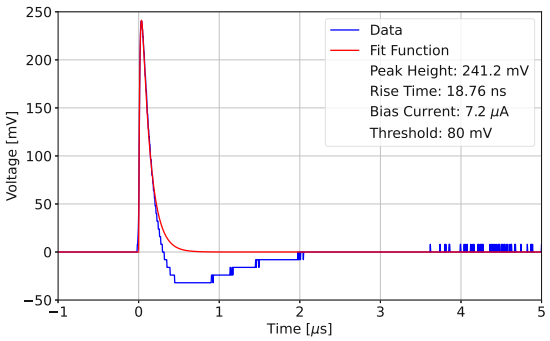

Figure A.20.: SiPM pos.: AB34

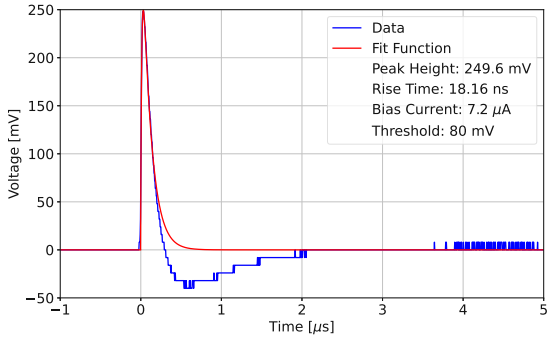

Figure A.21.: SiPM pos.: CD12

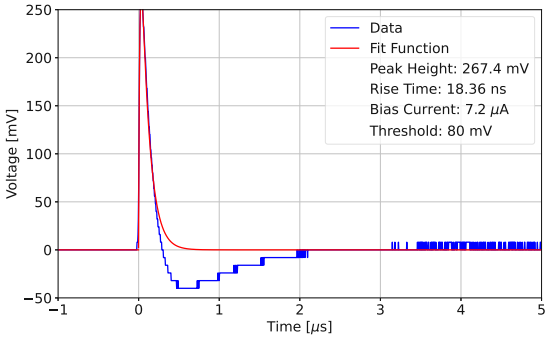

Figure A.22.: SiPM pos.: CD34

A.5. Whole Array, Source: ^{133}Ba

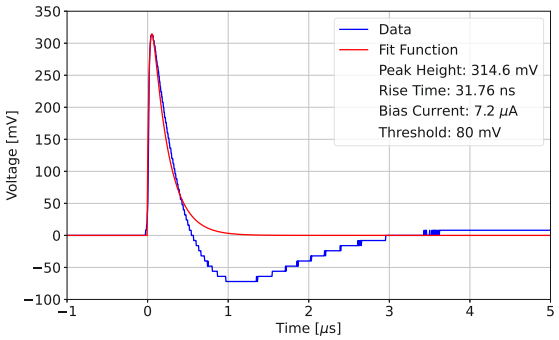

Figure A.23.: Measurement 1

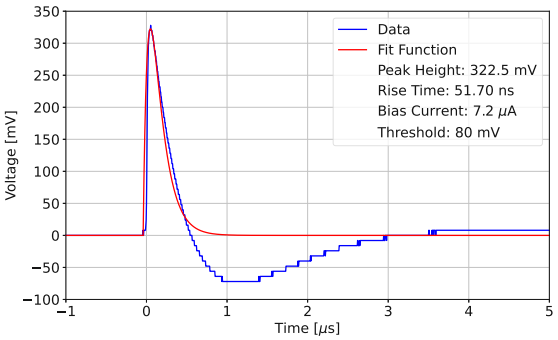

Figure A.24.: Measurement 2

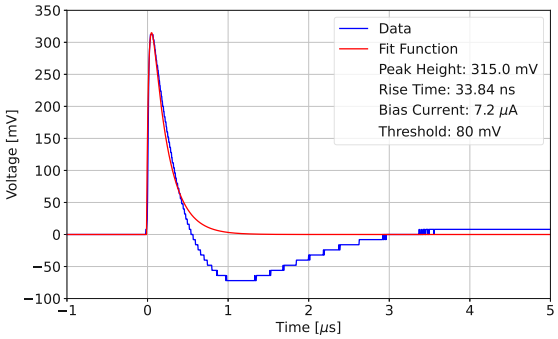

Figure A.25.: Measurement 3

B. Pre-Trigger Noise

B.1. Short vs. Long Cables (I_{bias}=7.2 µA, BC-408, ^{137}Cs Source)

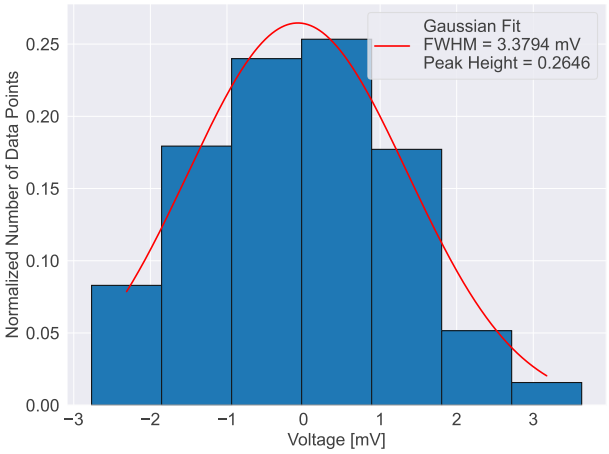

Figure B.1.: Short cable, SiPM pos.: A1

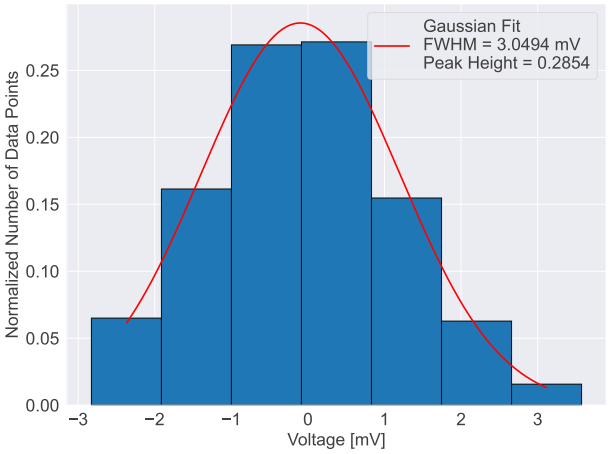

Figure B.2.: Long cable, SiPM pos.: A1

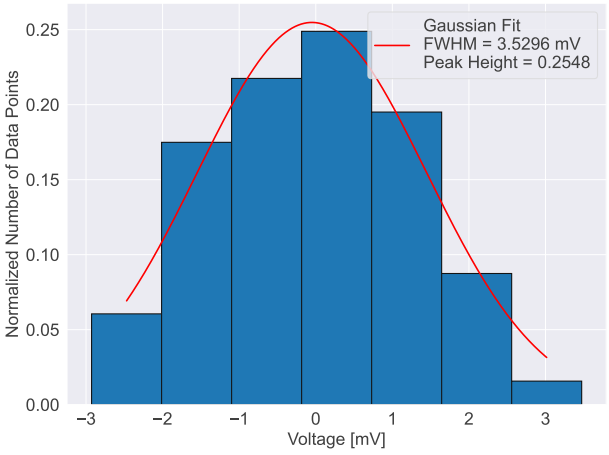

Figure B.3.: Short cable, SiPM pos.: A3

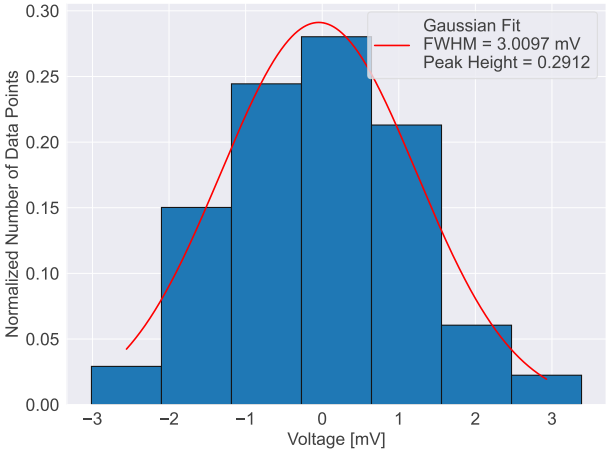

Figure B.4.: Long cable, SiPM pos.: A3

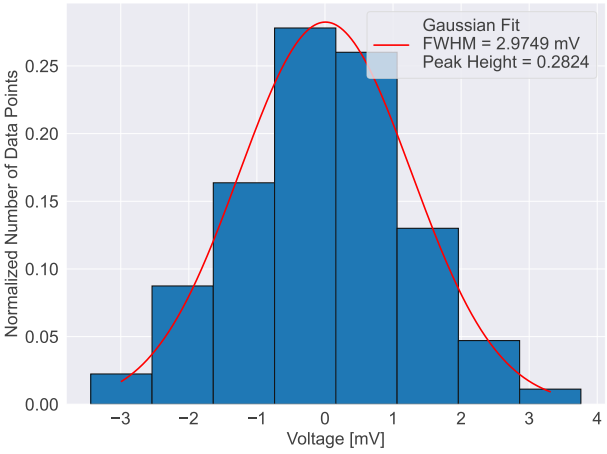

Figure B.5.: Short cable, SiPM pos.: B2

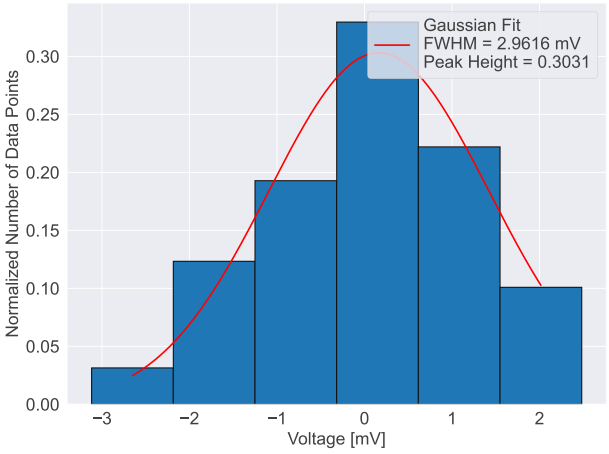

Figure B.6.: Long cable, SiPM pos.: B2

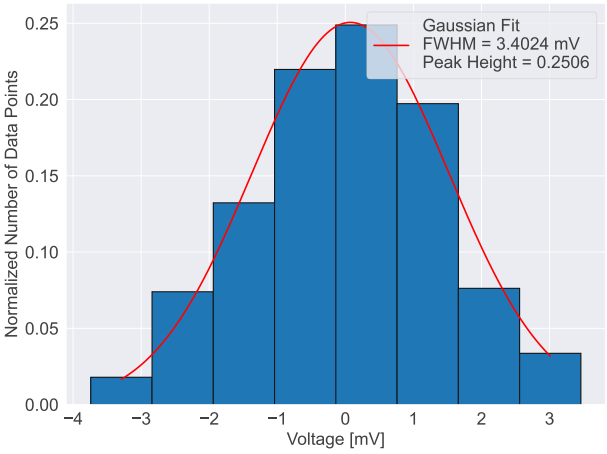

Figure B.7.: Short cable, SiPM pos.: B4

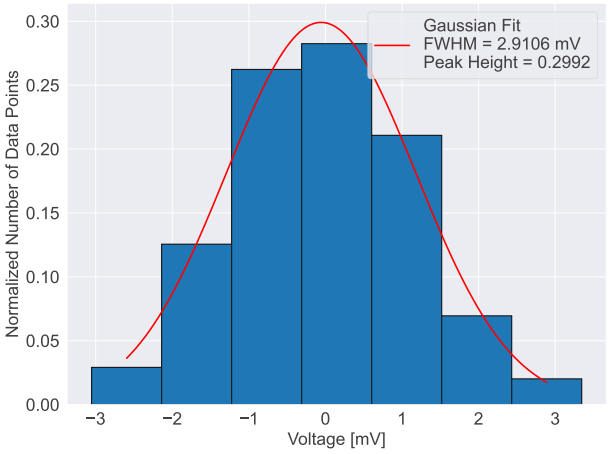

Figure B.8.: Long cable, SiPM pos.: B4

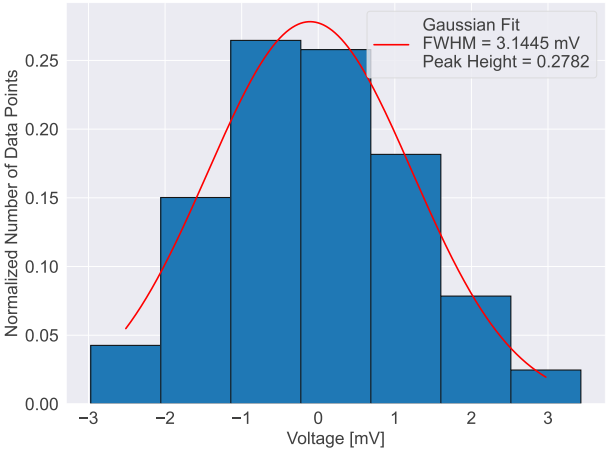

Figure B.9.: Short cable, SiPM pos.: C1

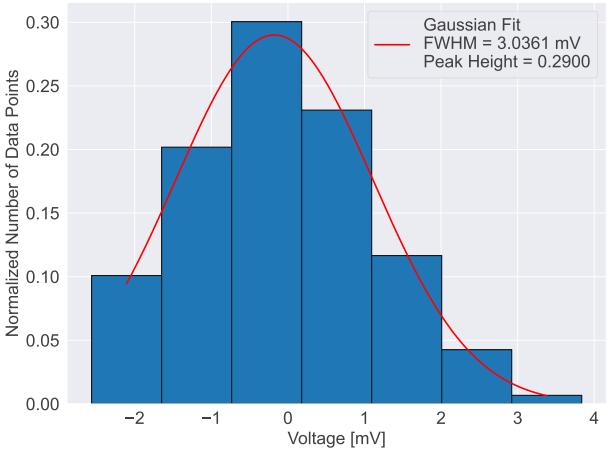

Figure B.10.: Long cable, SiPM pos.: C1

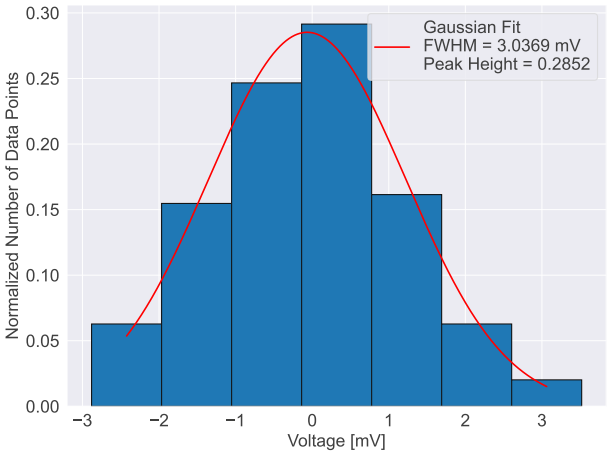

Figure B.11.: Short cable, SiPM pos.: C3

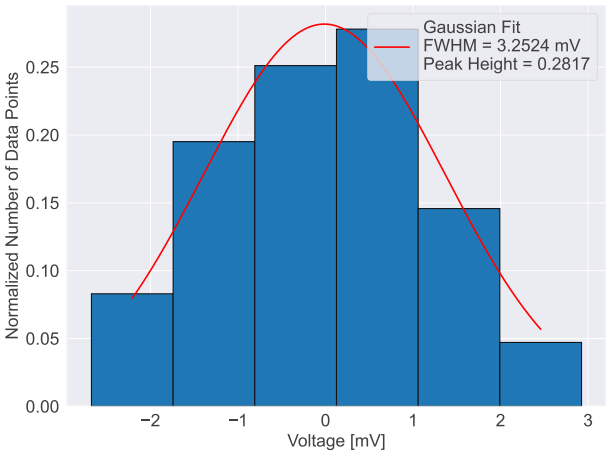

Figure B.12.: Long cable, SiPM pos.: C3

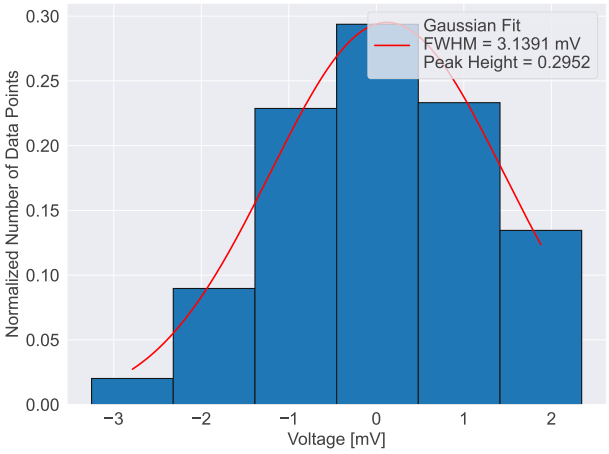

Figure B.13.: Short cable, SiPM pos.: D2

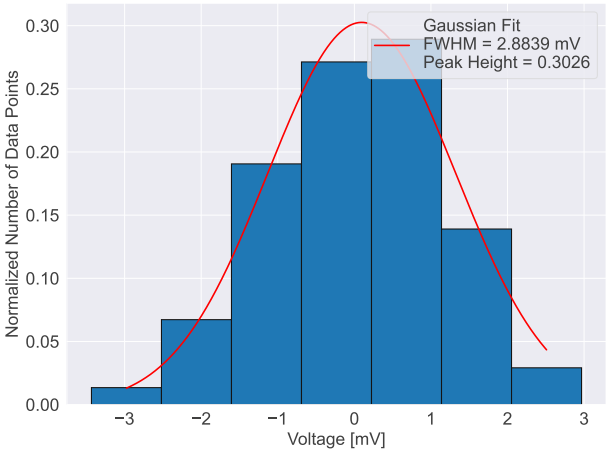

Figure B.14.: Long cable, SiPM pos.: D2

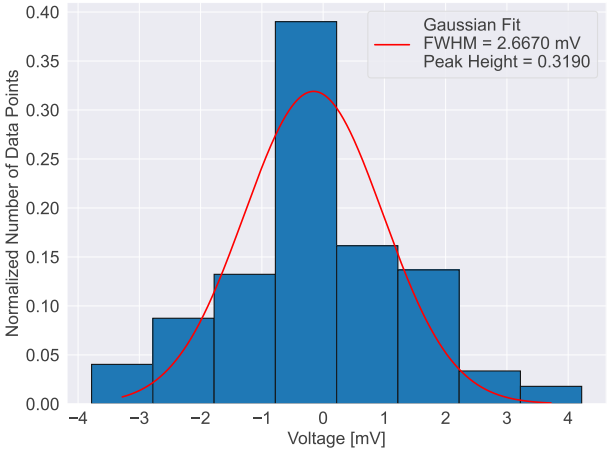

Figure B.15.: Short cable, SiPM pos.: D4

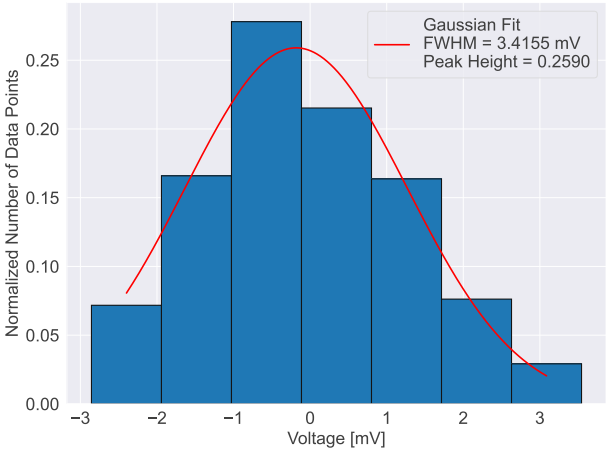

Figure B.16.: Long cable, SiPM pos.: D4

B.2. Individual vs collective Read-out

B.2.1. Individual ($7.2\,\mu A$, BC-408, ^{133}Ba Source)

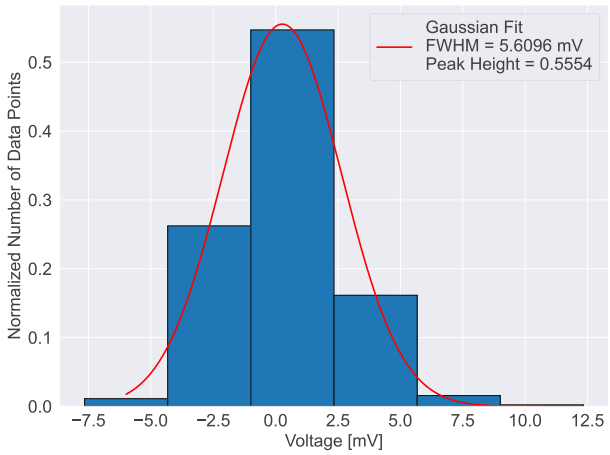

Figure B.17.: SiPM pos.: A1

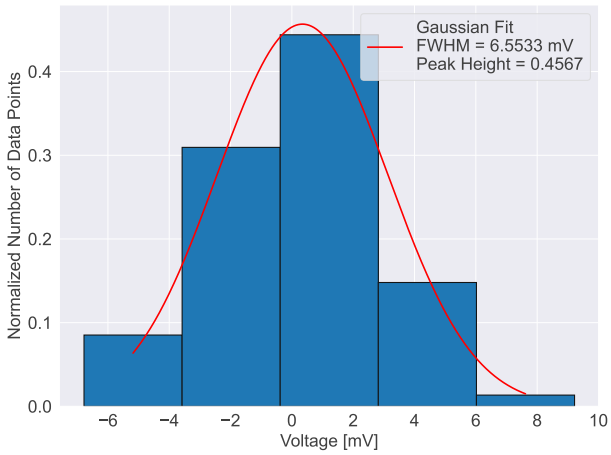

Figure B.18.: SiPM pos.: A2

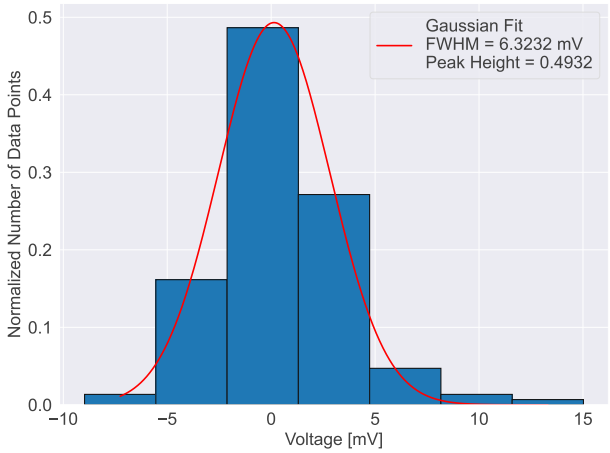

Figure B.19.: SiPM pos.: B1

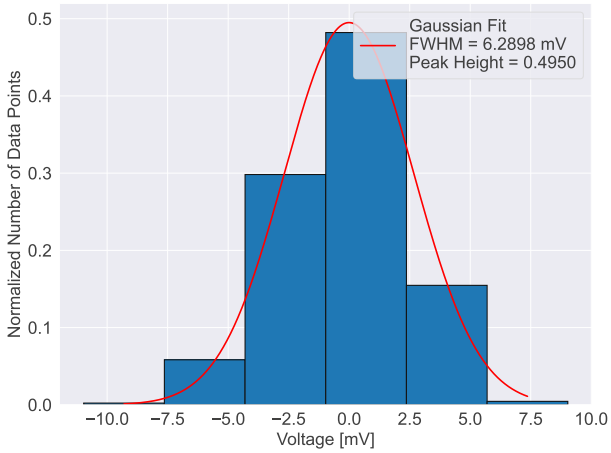

Figure B.20.: SiPM pos.: B2

B.2.2. Groups of Four

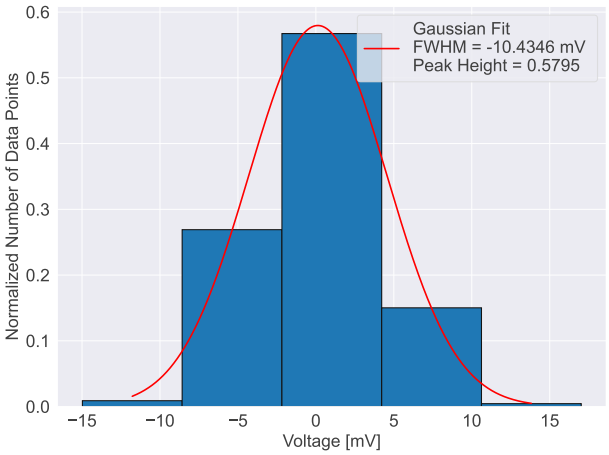

Figure B.21.: SiPM pos.: AB12

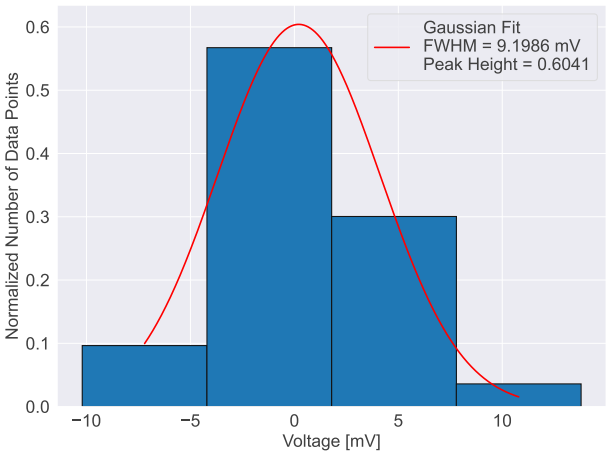

Figure B.22.: SiPM pos.: AB34

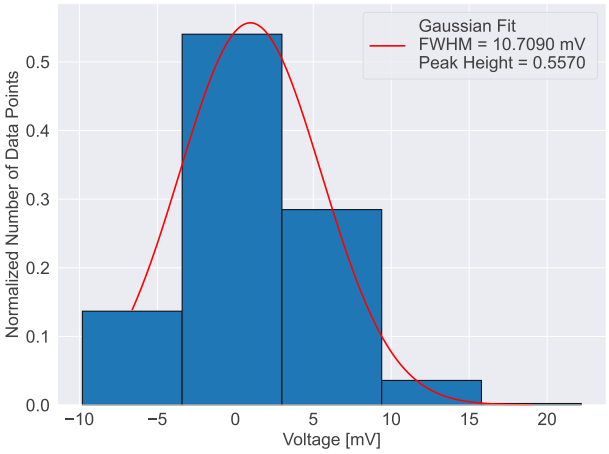

Figure B.23.: SiPM pos.: CD12

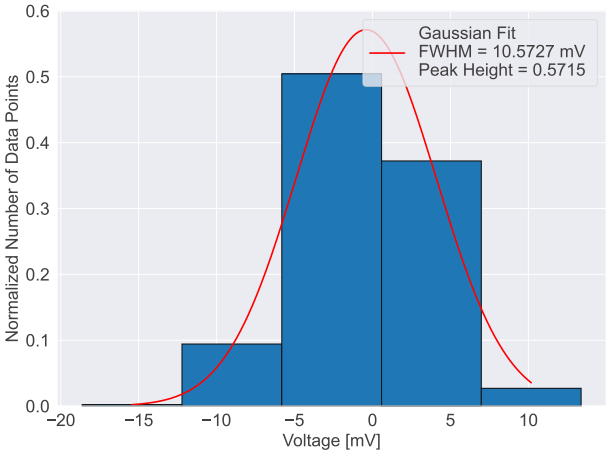

Figure B.24.: SiPM pos.: CD34

B.2.3. Whole Array

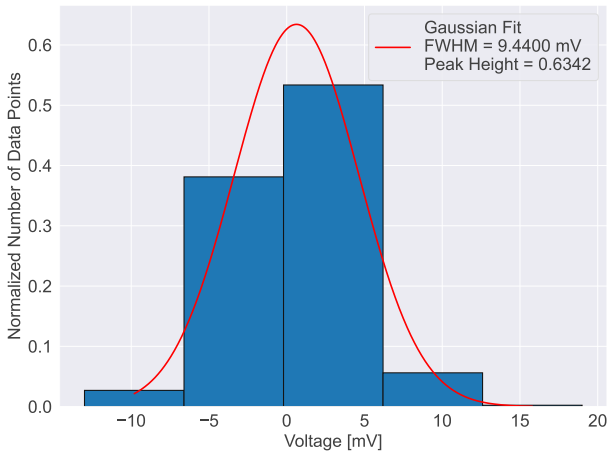

Figure B.25.: Measurement 1

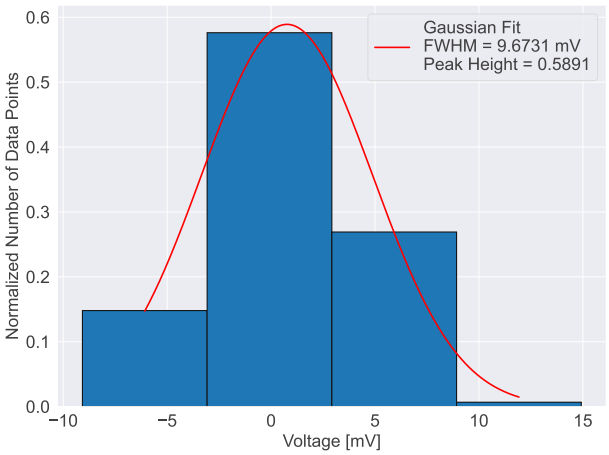

Figure B.26.: Measurement 2

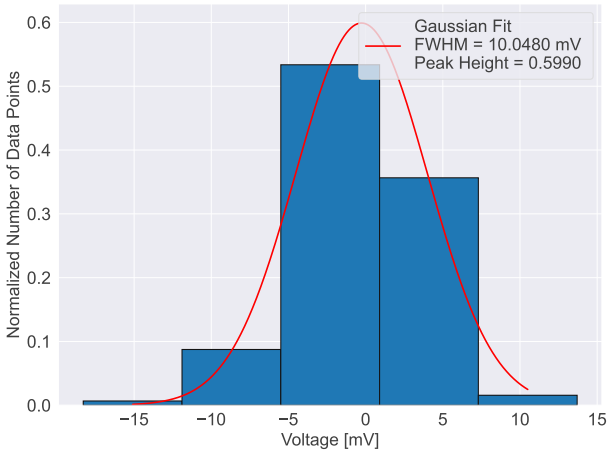

Figure B.27.: Measurement 3